Late Cretaceous erosion and chemical weathering record in the offshore Cape Basin: source-to-sink system from Hf Nd isotopes and clay mineralogy.

Camilo E. Gaitan, Emmanuelle Pucéat, Pierre Pellenard, Justine Blondet, Germain Bayon, Thierry Adatte, Claudine Israel, Cécile Robin, François Guillocheau

Marine Geology 466 (2023) 107187

Contents lists available at ScienceDirect

Marine Geology

journal homepage: www.elsevier.com/locate/margo

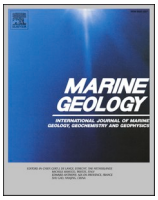

Late Cretaceous erosion and chemical weathering record in the offshore Cape Basin: Source-to-sink system from Hf—Nd isotopes and clay mineralogy

Camilo E. Gaitan [a,*], Emmanuelle Pucéat [a], Pierre Pellenard [a], Justine Blondet [a], Germain Bayon [b], Thierry Adatte [c], Claudine Israel [d], Cécile Robin [e], François Guillocheau [e]

[a] UMR 6282 Biogéosciences, Université de Bourgogne - CNRS, Dijon, France.
[b] Unité de Recherche Géosciences Marines, IFREMER, Plouzané, France
[c] ISTE, Université de Lausanne 1, Lausanne, Switzerland
[d] Institut de Physique du Globe de Paris (IPGP) - Université Paris Cité – CNRS, Paris, France
[e] Géosciences Rennes, Université de Rennes 1, UMR CNRS 6118, Rennes, France

ARTICLE INFO

Editor: Adina Paytan

Keywords:
Isotope geochemistry
Tectonics-climate
Clay mineralogy
South African Plateau
Paleoclimate

ABSTRACT

Source-to-sink research has often used sediment fluxes as a fundamental parameter when seeking to understand the perturbations caused by tectonics or climate. This parameter is often interpreted only in terms of erosion rates, dismissing the component exerted by chemical weathering. In this study, we characterize sediments from the Deep Surface Drilling Program core 361 (DSDP 361) located in the Cape basin to show the evolution of both, physical erosion and silicate chemical weathering, during the late Cretaceous (100.5–66 Ma) in the source-to-sink system consisting of the South African plateau and the Cape Basin. Transmission Electron Microscopy (TEM) images and trace element analyses indicate that detrital clays predominate within the site and thus reflect variations in surface continental processes. Clay mineralogy shows a predominance of detrital smectite (60–98%) throughout the section. However, an increase in primary clay minerals, in particular illite (20%), indicates a relative enhancement in physical erosion, while an increase in palygorskite (10%) indicates regional climate aridification during the Campanian–Danian interval (ca. 77–62 Ma). Concomitant to this enhancement, we observe both, more radiogenic Hf isotopic compositions and less radiogenic Nd isotopic compositions in the clay fractions (< 2 μm). These variations can be respectively associated to an increase in silicate chemical weathering and the incorporation of unradiogenic material, likely related to the orogenic belts present on the western-south margin of Southern Africa. The regional aridification and the global climate cooling trend observed on $\delta^{18}O$ benthic foraminifera records do not appear as suitable mechanisms for the increase in physical erosion and silicate chemical weathering observed. Our results, together with the reported increase in sedimentation rates and the reported tectonic uplift between 80 and 70 Ma, suggest that it is tectonic activity and not climate the main driver in the enhancement of denudation processes. Furthermore, our data suggests that such uplift episode could have impacted the regional climate by causing a rain-shadow effect, with an inland aridification suggested by the increase in palygorskite proportions. The increase in silicate chemical weathering suggested by our new dataset begins in the Campanian (ca. 77 Ma), later than the onset of the global climatic cooling trend that occurs from the Turonian onward. If enhanced weathering of the South African Plateau may not have triggered the recorded climatic cooling, it may still have contributed to maintain cooler conditions in the Campanian-Danian interval.

1. Introduction

In deep time source-to-sink systems ($\geq 10^7$ years) source and transfer zones are rarely preserved, thus sedimentary archives become the best and sometimes the only available record to study changes caused by environmental perturbations in source-to-sink systems. The way such

* Corresponding author.
E-mail address: camilo-esteban.gaitan-valencia@u-bourgogne.fr (C.E. Gaitan).

https://doi.org/10.1016/j.margeo.2023.107187
Received 4 August 2023; Received in revised form 30 October 2023; Accepted 19 November 2023
Available online 22 November 2023

changes are propagated and recorded is often interpreted by studying sediment fluxes (e.g., Allen and Densmore, 2000; Armitage et al., 2013; Castelltort and Van Den Driessche, 2003). These fluxes are primarily governed by tectonic and climatic boundary conditions that subsequently determine the intensity of denudation processes (Romans et al., 2016; Tofelde et al., 2021), essentially erosion and chemical weathering (Frank and Arthur, 1999; Herman et al., 2013). Although several studies have addressed sediment fluxes to understand the dynamics of climate and tectonics (e.g., Adams et al., 2020; Whipple, 2014; Whipple and Meade, 2006), most of them have focused on the control exerted by erosion rates without major consideration of the silicate chemical weathering role. Therefore, the use of proxies tracing the evolution of silicate chemical weathering compared to erosion appears to be of prime importance to access key mechanisms governing sediment supply, environmental signals, and tectonic-climatic forcings within deep time source-to-sink systems.

To study the evolution of such denudation processes, we have chosen the source-to-sink system composed by the South African Plateau and the Cape basin. The timing and processes that led the plateau to have a high elevation – low relief configuration are still debated, but multiple thermochronological analyses, landscape modelling, and sedimentological analyses (see compilation table in Stanley et al., 2021), have suggested that tectonic uplift played a significant role in the development of such configuration, primarily during the mid-late Cretaceous (~113–66 Ma) (Baby et al., 2019; Braun et al., 2014; Flowers and Schoene, 2010; Kounov et al., 2013; Wildman et al., 2017). Furthermore, this uplift episode occurred during a greenhouse climate period (Friedrich et al., 2012; Huber et al., 2018), just at the onset of a long-term global cooling trend that began in the late Cretaceous (ca. 93 Ma) (Friedrich et al., 2012; O'Brien et al., 2017; Zachos et al., 2008).

The aim of this study is to constrain the record of silicate chemical weathering and physical erosion along the South African Plateau during the late Cretaceous (100.5–66 Ma; Gradstein et al., 2012), also by exploring how the changes in such record are linked to climate and/or tectonic forcings. Here, we analysed 99 samples from the Deep-Sea Drilling Project core 361 (DSDP 361) located in the Cape basin (Fig. 1). We applied a new proxy based on Hf – Nd isotopic compositions in clay fractions (< 2 μm - Bayon et al., 2016) to track changes in silicate chemical weathering, and combined it with X-ray diffraction (XRD) analyses, transmission electron microscopy images (TEM), and major and trace element analyses, to determine the nature and changes in sources, denudation rates, and the evolution of denudation processes in relation to climate and/or tectonic forcings.

2. Regional setting

2.1. Geological setting

Multiple scenarios have been invoked to explain the current topographic configuration of the South African Plateau (see Baby et al., 2019). Recently, Stanley et al., 2021 combined geomorphological, thermochronological, and sedimentological data through landscape modelling to narrow down these scenarios into the two most feasible. In the first scenario, most of the topographic development occurs between

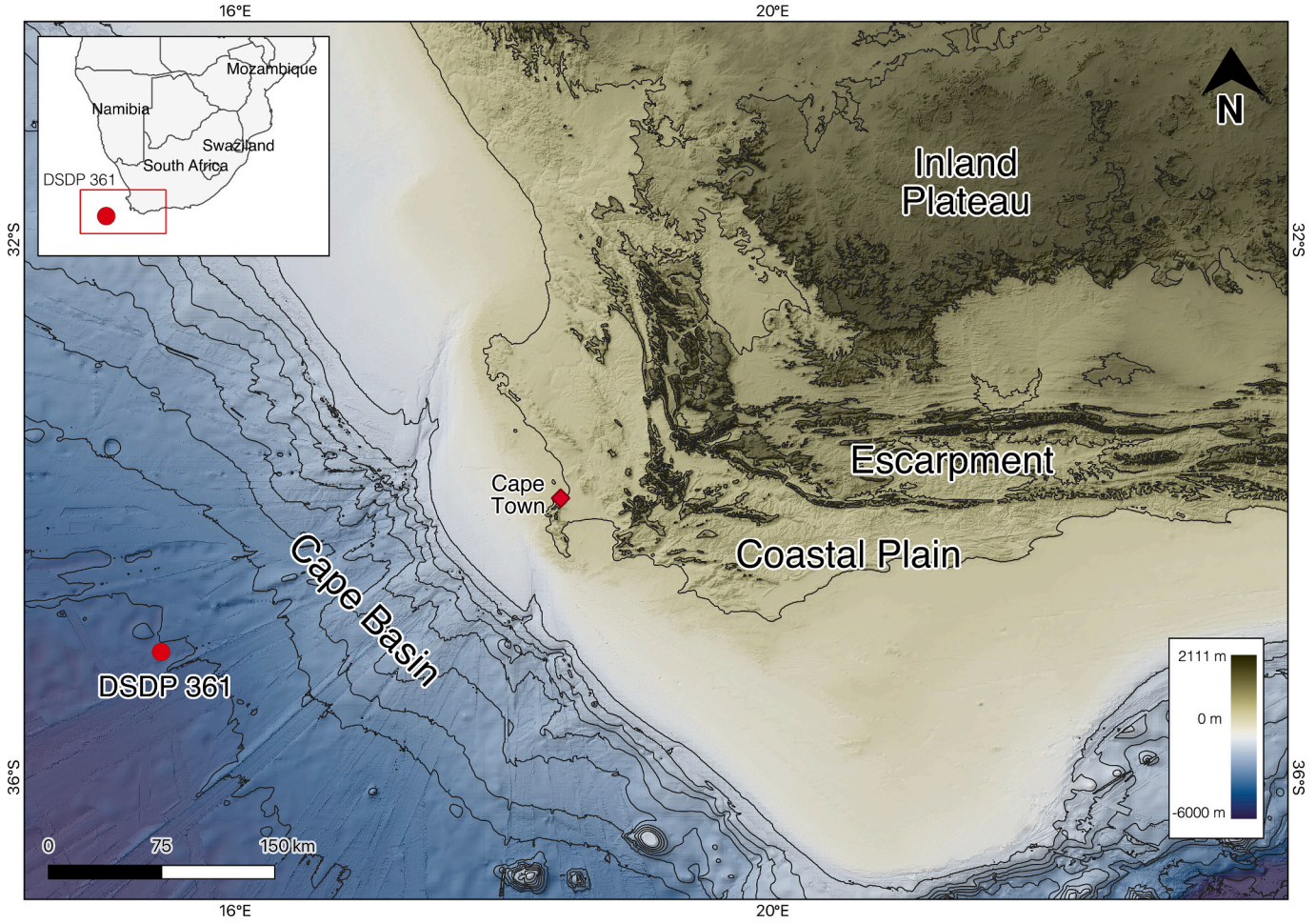

Fig. 1. South-western topographic-bathymetric map of the source-to-sink system composed by the South African plateau and the Cape basin. DSDP core 361 (35°03.97′S; 15°26.91′E) is located in the abyssal plain of the Cape basin. Topography and bathymetry data compiled from NASA (2013).

90 and 100 Ma, and it is linked to tectonic uplift and continental tilting. In the second scenario, although there is also a component of uplift and tilting during such period (ca. 400–800 m), it includes a significant component of uplift during the mid-Cenozoic (ca. 23 Ma; 500–1000 m). Regardless the scenario, tectonic uplift during the Cretaceous (ca. 100–70 Ma) has been commonly suggested because it better explains the denudation periods and contrasting sedimentation rates in the basins adjacent to the margin during this period (Baby et al., 2019).

The current drainage configuration in the plateau is mainly dominated by the Orange river system (Fig. 2), but some changes in the catchment configuration have been reported since the Cretaceous (De Wit et al., 2009; De Wit, 1999; Dollar, 1998; Goudie, 2005). De Wit et al. (2009) proposed two paleorivers during the mid-late Cretaceous (113–66 Ma), the Karoo and Kalahari rivers. The Karoo River is suggested to have drained southern areas of the plateau and had an outlet correspondent to the modern Olifants river. On the other hand, the Kalahari River drained northern areas (Botswana-Namibia) and flowed toward the Atlantic in a similar path to the modern Orange river outlet. However, by the early Cenozoic (ca. 60 Ma), both river systems had merged into one giving place to the modern Orange river system, a process that has been attributed to accelerated tectonic uplift (De Wit et al., 2009; De Wit, 1999). This indicates that sediments deposited in the Cape Basin during the late Cretaceous (93.9–66 Ma) likely encompass an extensive area of the plateau, by potentially receiving sediments through the Karoo paleoriver, which drained a more extensive area compared to the modern Olifants river system that feeds the basin nowadays (Fig. 2).

The set of geological units that comprise the South African Plateau were the main detrital input into the Cape Basin during the late Cretaceous (Fig. 2) The oldest units are located at the eastern margin comprising the Kaapvaal Craton (3.7–2.7 Ga) and the Limpopo belt (3.3–2.6 Ga; Schlüter, 2008; Tankard et al., 1982). This craton is a heterogeneous province composed mainly of granitoids intruding greenstone belts of volcanic and sedimentary origin (Eglington and Armstrong, 2004), whereas the Limpopo belt consists of granulitic and amphibolitic metamorphic rocks. Orogenic belts predominate in the western margin of the plateau. The Namaqua-Natal orogen (2.2–1 Ga) comprises a Paleoproterozoic basement of volcanic and sedimentary sequences, while the Cape Belt (546–251 Ma) at the southern of the margin consists of a Paleozoic succession of low-grade metasediments, mainly mudstones, sandstones, and glacial deposits. The Saldania belt, known as the southernmost segment of the Damara orogen consists of volcano-sedimentary sequences with multiple granitic intrusions (0.55–0.5 Ga; Chemale et al., 2011). In the central part of the plateau are located two extensive basins, the Karoo and Kalahari basins. The former encompasses thick sedimentary sequences deposited between the upper Carboniferous and the lower Jurassic (298–174 Ma), when the extrusion of the Karoo flood-basalts marked the end of deposition (Dia et al., 1990; Svensen et al., 2012). The latter consists of extensive pedogenically affected sand and gravel deposits dated back to the late Cretaceous (~88 Ma) (Haddon and McCarthy, 2005).

Sediment accumulation in the Cape basin is reported since the Aptian (~120 Ma) (Bolli et al., 1978). Sediments deposited in this period correspond to sandy mudstones and sapropelic shales with high carbonate content, interpreted as deep-proximal fan to fan-valley facies (Bolli et al., 1978). Conversely, sediments deposited during the Albian-Maastrichtian (113–72.1 Ma) interval consist of more extensive shales, poor in carbonate content, and intercalated with thin sandy mudstones, corresponding to distal fan turbidite facies deposited under the carbonate compensation depth (CCD), and with minor influence of deep-bottom currents (Natland, 1978). By the Danian (66–61.6 Ma), the predominant lithology are mudstones, indicating a shift to more predominant pelagic deposition.

2.2. Climate setting

Climate evolution in the South African Plateau during the late Cretaceous has been inferred by regional palynological studies compiled

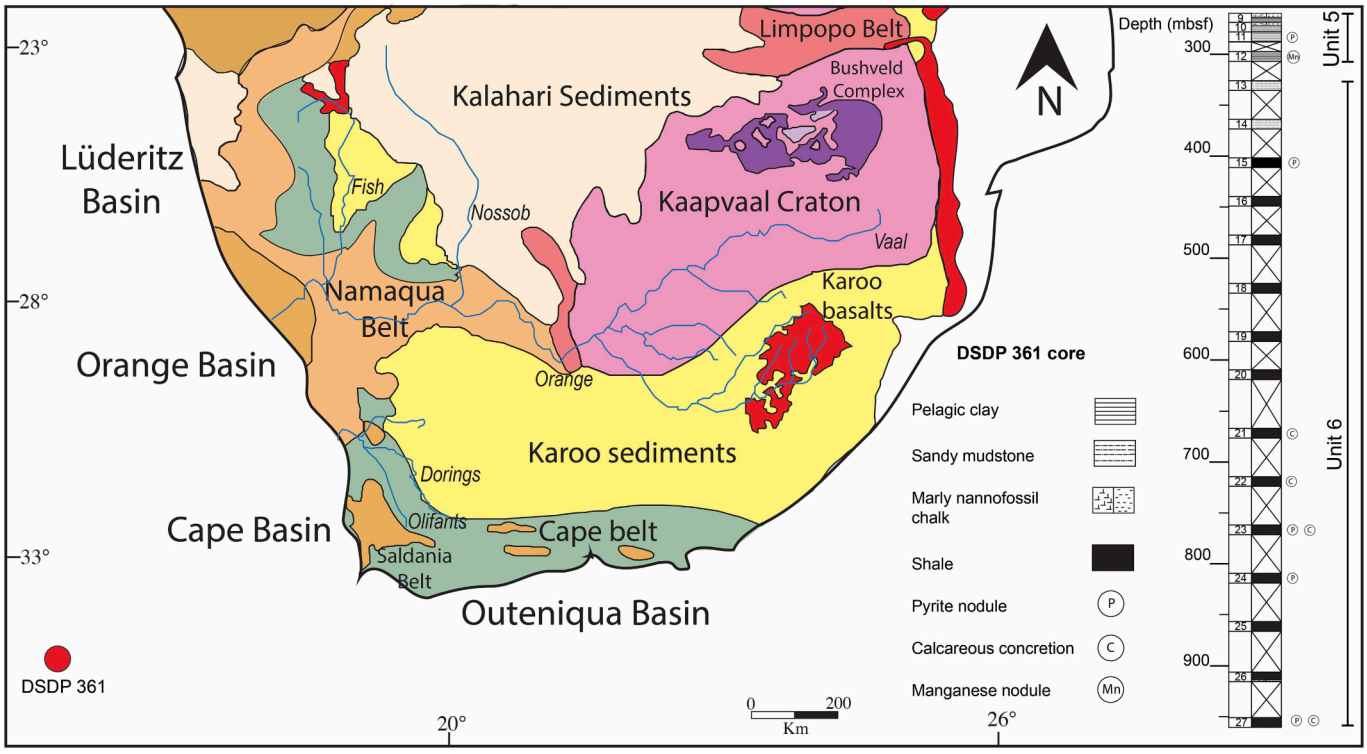

Fig. 2. Main geological units, river tributaries, and basins at the South-western margin of South Africa. Modified after Garzanti et al. (2014). DSDP 361 core log shows the lithology of the studied units. *Mbsf = meters below sea floor*. Crossed boxes represent void sections within the core. River tributaries: *Fish, Nossob, Orange, Vaal, Olifants, Dorings*.

in Braun et al. (2014). Although rather localized, fossil assemblages recovered from continental sections in the inner Plateau indicate that by the mid-Cretaceous (ca.100 Ma) the climate was tropical to subtropical, with temperate, seasonal, and predominantly wet conditions (Bamford and de Wit, 1993; Bamford and Stevenson, 2002; Rayner et al., 1997). According to Braun et al. (2014), a shift to more semi-arid conditions is recorded by the end of the Cretaceous (ca. 70 Ma), based on palynological data from continental sites located in the Plateau (Smith, 1988, 1986) even though the sites are located relatively far apart from each other. Paleoflora studies in offshore areas show predominant tropical, humid, temperate conditions during the early Cretaceous (~130 Ma), however a shift into warmer semi-arid conditions is observed by the mid-Cretaceous (ca. 95 Ma) (Sandersen, 2006). By the end of the late Cretaceous (66 Ma), they suggest that climatic conditions would have shifted back to warm and humid (Sandersen, 2006).These contrasting changes show that even during the global cooling trend that started in the Cretaceous (Friedrich et al., 2012; O'Brien et al., 2017; Zachos et al., 2008) regional climate dynamics could have caused some episodic warming periods and variations in precipitation regimes. These studies, although remaining sparse and localized, suggest the existence of a contrast in climatic conditions when comparing onshore to offshore data, hinting at different climatic regimes for the offshore and onshore settings.

3. Material and methods

3.1. Core description

The samples analysed in this study belong to the DSDP core 361 (465.5 m) located in the abyssal plain of the Cape Basin, offshore the south-western part of the South African Plateau (Figs. 1 and 2) This core consists of a stratigraphic section ranging from Aptian to upper Eocene (Bolli et al., 1978), and represents the stratigraphic continuation of the DSDP core 360 that spans from Pliocene to middle Eocene (Bolli et al., 1978). The whole stratigraphic section (DSDP 360 and 361) is divided in 7 lithological units from which DSDP core 361 encompasses unit 4 to 7, subdivided in 49 cores of 9.5 m each (Bolli et al., 1978). In this study, we analysed 99 samples from units 5 and 6 (Figs. 2 and 3; core 9–27) covering Albian to Danian deposits (Supplementary table S1). The lithology in Unit 5 (cores 9 to 12) is mainly composed by pelagic clays with sporadic intercalations of marly nannofossil chalk and seldom pyrite nodules. In Unit 6 (cores 12 to 28) shales are predominant, only with some minor thin intercalations of sandy mudstones. Some calcareous concretions and pyrite nodules are also reported (Bolli et al., 1978). Davey, 1978

The selected samples were targeted considering even distribution within the studied time interval (i.e., the late Cretaceous; 93.9–66 Ma) and rich clay content. However, the position of age boundaries within the interval presents some uncertainties due to a relative lack of foraminifera and nannofossil fauna. Boundaries are defined by a combination of the latter when present (Bolli et al., 1978), and marine palynomorphs (i.e., dinocysts and acritarchs; Davey, 1978). The Aptian-Albian boundary is defined in core 27 (954.3 mbsf) by the last occurrence of *Muderongia staurota* (Davey, 1978). The transition between Early and Late Cretaceous is relatively well defined by the presence of calcareous nannofossils, this transition is placed in core 26 (905.5–915 mbsf) due to the occurence of *Prediscosphaera cretacea* in this core (Bolli et al., 1978). Fauna from the Cenomanian was not identified in this core, suggesting this interval is either barren or absent. The base of the Turonian (93.9 Ma) is defined in core 24 (810,5–820 mbsf), marked by the first occurrence of *Florentinia resex* (Davey, 1978). Although the presence of *Hystrichisphaeridium spiniferites* is indicative of Coniacian fauna, the Turonian-Coniacian boundary is not well identified, and we tentatively placed it between cores 21 and 20 (610,5–677,5

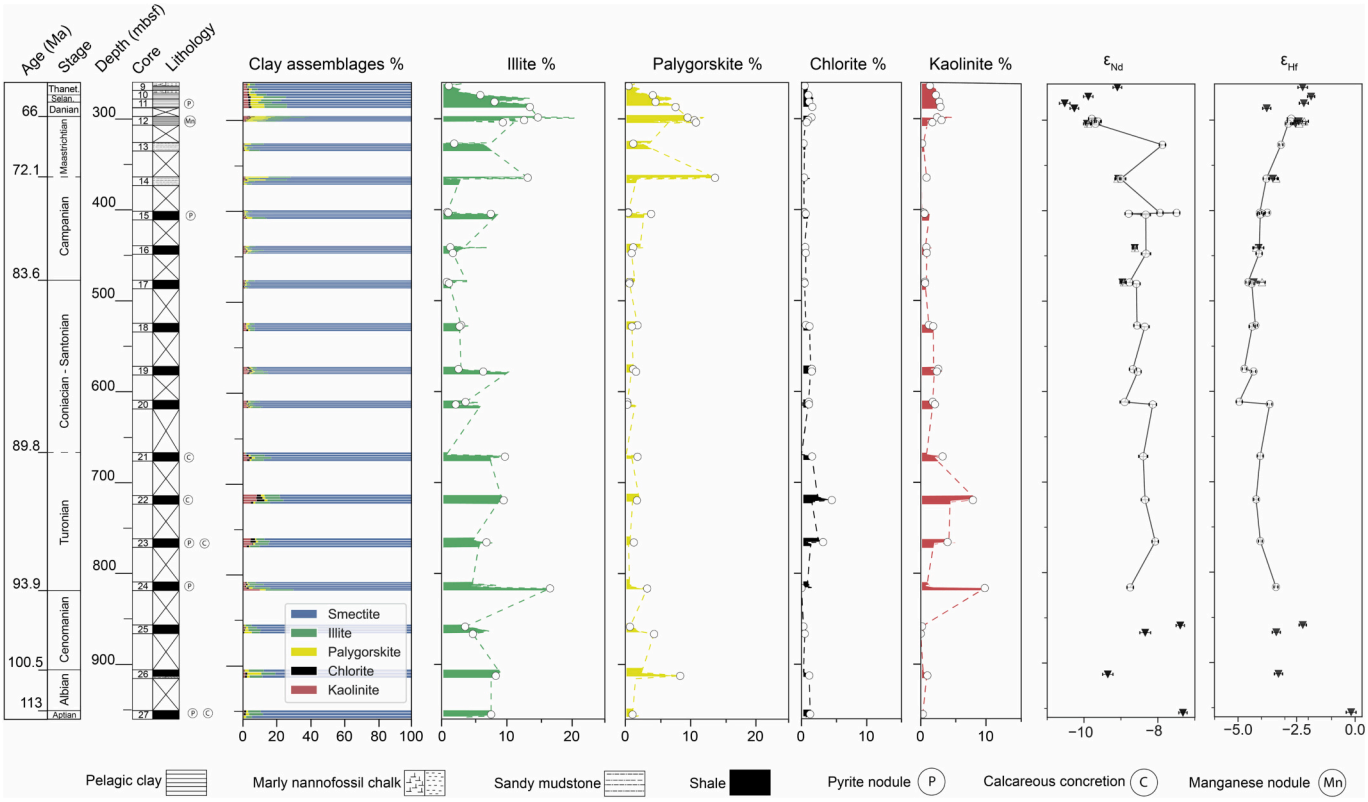

Fig. 3. Lithology, clay assemblages, and present-day ε_{Nd}.ε_{Hf} isotope compositions of the studied samples of the DSDP core 361. White circles (also in the clays plots) represent the samples measured for Hf – Nd isotopic compositions. Inverted grey triangles represent replicates that were analysed for Hf—Nd isotopes by automated column chromatography and acid treatment. White triangles represent replicates using alkaline fusion and automated column chromatography.

mbsf). Likewise, the Coniacian-Santonian boundary is not properly defined, but the last occurrence of *Dinopterygium cladoides* (574.5 mbsf) at core 19 defines already a Santonian age (Davey, 1978). The Santonian-Campanian boundary is defined at core 17 (479.5 mbsf) by the last occurence of *Hystrichodinium pulchrum* and *Palaeohystrichosphora infusorioides* (Davey, 1978). There are not fossil assemblages that enable to identify the Campanian-Maastrichtian boundary, but the Maastrichtian-Danian boundary is placed in core 12 (297 mbsf) based on the last occurrence of *Odontochitina porifera* in core 13 (Davey, 1978) and the first occurrence of *Cruciplacolithus tenuis* in core 10 indicating already Paleocene ages (278 mbsf; Bolli et al., 1978).

Based on these fossil assemblages, age's intervals and boundaries were established following the *Geological Time Scale 2012* (Gradstein et al., 2012). An age model was built using linear regressions between five tie-points (Supplementary material FS1): the Aptian-Albian boundary (854.3 mbsf), the Cenomanian-Turonian boundary (820 mbsf), the Turonian-Coniacian boundary (620 mbsf), the Santonian-Campanian boundary (479.5 mbsf), and the Maastrichtian-Danian boundary (297 mbsf).

3.2. Analytical techniques

3.2.1. X-ray diffraction (XRD) analyses

XRD analyses were carried out on whole rock and clay fractions in the Biogeosciences Laboratory of Dijon (UMR CNRS 6282) at the University of Burgundy, France. Ninety-nine samples (Supplementary table S1) were analysed on a Bruker D8 Endeavor diffractometer with Cu-Kα radiations, a LynxEye detector coupled to a Ni filter, and under a 40-kV voltage with 25-mA intensity. Semi-quantitative estimations from the resulting diffractograms were calculated using the MacDiff software 4.2.5 (Petschick, 2001) to determine the main intensity peaks. Oriented glass slides were measured three times following the protocol set by Moore and Reynolds (1989), including both ethylene glycol and heating (490 °C) preparation stages. Using the MacDiff software 4.2.5, clay mineral proportions were determined by calculating the area of the basal reflections (d_{001}). This calculation was done using the resulting diffractograms from the ethylene glycol treatment (Moore and Reynolds, 1989).

3.2.2. Transmission Electron Microscopy (TEM) observations

TEM analyses were performed on clay fractions from 5 samples (Supplementary table S1) at the Applications, Research, and Characterization at the Nanometric scale analysis centre (ARCEN) of Dijon, at the University of Burgundy, France. The samples were dispersed in distilled water and 2% *v/v* butylamine solution, and then set on a carbon formvar Cu grid. Images were taken using a JEOL JEM 2100F, and EDX chemical analyses were performed with the equipped Bruker Xflash Detector 5030 spectrometer.

3.2.3. X-ray fluorescence (XRF) analyses

Major and minor oxide abundances were determined for 97 samples (Supplementary table S1) by XRF at the Institut Sciences de la Terre, at the University of Lausanne, Switzerland. To perform the measurements, fused disks were prepared from 1.2 g of calcined sample powder mixed with Lithium-Tetraborate (1:5 proportions). The measurements were done using a wavelength dispersive PANalytical Axios^{mAX} spectrometer fitted with a 4 kW Rh X-ray tube, and rock silicate reference materials were used for calibration.

3.2.4. Chemical processing for trace element and isotopic analyses

After an initial grinding stage, 1.3 to 1.5 g of sample powder was sequentially leached using a procedure based on the protocol described in Bayon et al., 2002 and Gutjahr et al., 2007. Carbonates were first removed using 10% v/v acetic acid overnight. The Fe—Mn oxyhydroxide phases were then removed using a 0.5 M hydroxylamine hydrochloride solution in 20% v/v acetic acid for 48 h. Finally, organic matter was removed with a 48-h step in 5% H_2O_2. After these leaching stages, the clay fractions were extracted using particle decantation for 1 h and 35 min according to the Stokes law.

The leached samples were dried and processed by alkaline fusion according to the protocol outlined in Bayon et al., 2009, along with 5 certified reference standards (BHVO-2, BIR-1, MAG-1, BCR-1, and BCR-2) from the United States Geological Survey (USGS). Approximately 75 mg of each sample were placed into carbon crucibles together with 0.5 g of Tm spike, 0.6 g of NaOH, and 1.2 g of Na_2O_2. The crucibles were heated at 650 °C for 12 min in a furnace, before being cooled down with ultrapure 18.2 MΩ water, resulting in the precipitation of Fe-hydroxides. The samples were then centrifuged, and finally dissolved in 3,3 ml of 6 M HCl (this solution is referred onwards as mother solution). From such solution 0.3 ml were separated for trace elements analyses. The Tm spike was added as an internal standard in the quantification of trace elements following the method described in Barrat et al., 1996.

3.2.4.1. Trace elements. Trace elements concentrations were measured by inductively coupled plasma mass spectrometry (ICP-MS) on a Thermo Scientific X-Series II®, at the Pole Spectrométrie Océan of Brest, France (Supplementary table S2). Samples were diluted in 0.5 M HNO_3 solutions with a dilution factor of ~3000 (Barrat et al., 1996). We used standard bracketing and the Tm spike to precisely quantify trace elements as described in Barrat et al., 1996 and Freslon et al., 2011. Accuracy control and reproducibility was assessed analysing 4 of the USGS certified reference standards: BHVO-2, BIR-1, MAG-1, and BCR-2 (Supplementary table S3). Deviations from the reference standards (Bayon et al., 2009; Jochum et al., 2016; Smirnova et al., 2010) were below 16%, with exceptions for Gd in the standard MAG-1 (25% deviation), and Ba in the standard BIR-1 (59% deviation). Variability among the standards replicates was always below 9%.

3.2.4.2. Hf—Nd Isotopic analyses and measurements. Extraction of Hf and Nd for 22 samples was done using conventional column chromatography procedures described by Bayon et al. (2012) and Chu et al. (2002). The samples were divided into two aliquots processed separately for isolating Hf and Nd. Rare Earth Elements (REE) were first separated from the matrix using 3 ml of AG 50 W-X8 cationic resin (200–400 mesh) in 10 ml Biorad columns®. A second column using 1 ml of Ln Spec resin (50–100 μm) in 2 ml Biorad columns® was then used for purifying the Nd fraction. Hafnium was first separated from the matrix using 1 ml of AG 1-X8 anionic resin (200–400 mesh) in 10 ml Biorad columns®. A second column using 1 ml of Ln Spec resin (100–150 μm) in 2 ml Biorad columns® was finally used for purifying the Hf fraction.

During the course of this study, we also adapted the separation of Hf and Nd using the low pressure, automated column chromatography system PrepFAST-MC®, following the procedures from Chu et al. (2002); Garçon et al. (2018); Münker et al. (2001); and Pin and Zalduegui (1997). The PrepFAST® allows to implement sequentially automated separation protocols with customed single columns. Initially, Hf and REE were separated from the matrix using 2 ml of AG 50 W-X8 resin (200–400 mesh) in a customed 2 ml PFA PrepFAST® column (100 mm-long x 6.4 mm-diameter – see Table 1). From the REE fraction, Nd was purified using ≈1.8 ml of Ln Spec resin (600 mg of dry resin – 50-100 μm) in a customed 2 ml PFA PrepFAST® column (100 mm-long x 6.4 mm-diameter – see Table 1). Hafnium was finally purified using ≈0.8 ml of Ln Spec resin (300 mg of dry resin — 100-150 μm) in a custom 1 ml PFA PrepFAST® column (50 mm-long x 6.4 mm-diameter – see Table 1).

To verify consistency between conventional column chromatography and automated column chromatography, five samples were processed through both techniques and analysed afterwards. We also experienced the impact of using different digestion methods on the chemistry procedures and on the measured isotopic data. After the

Table 1
Detailed separation procedure for Hf and Nd extraction using the PrepFAST-MC® automated column chromatography system.

Elements eluted	Reagent	Volume (ml)	Elution speed (ml/min)
Step 1: Hf and REE separation from matrix			
2 ml-AG50W-X8 200–400 mesh resin			
Conditioning	1 M HCl	20	1.5
Load sample and collect Hf	1 M-HCl/0.1 M-HF	1	0.25
Collect Hf	1 M-HCl/0.1 M-HF	2	1
Major elements	2 M HCl	2 × 9	1.2
Collect REE	6 M HCl	5	1.5
Cleaning	0.05 M HCl	1	2
	2 M HF	2 × 5	1.5
	6 M HCl	5 × 5	1.5
Rinse and store	0.05 M HCl	2 × 5	1.5
Step 2: Nd purification			
600 mg-Ln Spec 50–100 μm resin			
Conditioning	0.2 M HCl	3 × 5	0.6
Load sample	0.2 M HCl	0.6	0.2
La, Ce, Pr	0.2 M HCl	2 × 6	0.6
Collect Nd	0.25 M HCl	9	0.6
Cleaning and elute HREE	6 M HCl	2 × 10	0.8
Rinse and store	0.05 M HCl	10	0.8
Step 3: Hf purification			
300 mg-Ln Spec 100–150 μm resin			
Conditioning	2.5 M HCl	3 × 5	2
Load sample	2.5 M HCl	5	0.6
Major elements	2.5 M HCl	10	2
	6 M HCl	10	2
Rinse	0.05 M HCl	4	2
Ti	0.4 M-HNO_3/0.09 M-$C_6H_8O_7$/1 wt% H_2O_2	6 × 10	1
Rinse H_2O_2	0.4 M-HNO_3/0.09 M-$C_6H_8O_7$	5	1.5
Zr	6 M-HCl/0.06 M-HF	5 × 10	1.5
Collect Hf	6 M-HCl/0.4 M-HF	4	1.5
Cleaning	2 M HF	3 × 10	1.5
	6 M HCl	3 × 10	2
Rinse and store	0.05 M HCl	2 × 10	2

leaching procedure, 50 mg of the leached sample's powder were acid digested instead of treated by alkaline fusion and then processed by automated column chromatography. After verifying consistency among the results, an additional set of 8 samples was treated by alkaline fusion and then processed with automated column chromatography to enlarge the data set.

Isotopic measurements (Table 2) were performed on 30 samples using a MC-ICP-MS Neptune Plus® (ThermoFisher-Scientific) at the École Normale Supérieure (ENS) of Lyon, France. Samples processed by both column chromatography procedures were measured at the ENS and the Magmas and Volcanoes Laboratory of Clermont-Ferrand, France. Reported errors are 2 standard deviation (2 sd).

Hafnium isotope measurements performed at the ENS consisted of a static acquisition method composed of 40 cycles, with average intensities of 6.7 and 9.5 V for sessions 1 and 2. Isotope ratios were corrected for mass bias through exponential law and using the stable isotope ratio $^{176}Hf/^{177}Hf = 0.7235$. Multiple measurements of JMC 475 solution (35 ppb) performed during the two sessions gave a ratio of $^{176}Hf/^{177}Hf = 0.282216 \pm 0.000007$ (24 ppm, $n = 18$) and $^{176}Hf/^{177}Hf = 0.282256 \pm 0.000007$ (24 ppm, $n = 21$) respectively. Samples were diluted at a similar concentration in 0.05 M HNO_3/ 0.001 M-HF solution. The resulting $^{176}Hf/^{177}Hf$ ratios were normalised to the reference value for JMC 475 $^{176}Hf/^{177}Hf = 0.282161$ (Vervoort and Blichert-Toft, 1999).

BHVO-2 and BCR-2 reference materials measured gave $^{176}Hf/^{177}Hf$ normalised isotopic values of 0.283101 ± 0.000007 (24 ppm, $n = 3$) and 0.282870 ± 0.000002 (7 ppm, $n = 4$) during session 1, and 0.283101 ± 0.000008 (28 ppm, $n = 5$) and 0.282868 ± 0.000002 (7 ppm, n = 2) during session 2. Both standards fit within the range of the reference values determined by Weis et al. (2005). Four procedural blanks for Hf were measured as well, obtaining values between 13 and 30 pg (Supplementary table S3).

Neodymium isotope measurements performed at the ENS consisted of a static acquisition method composed of 40 cycles, with an average intensity of 7.6 and 9.6 V respectively. Isotope ratios were corrected for mass bias through exponential law and using the stable isotope ratio $^{143}Nd/^{144}Nd = 0.7219$. Multiple measurements of JNDi-1 solution (40 ppb) performed during both sessions gave a ratio $^{143}Nd/^{144}Nd = 0.511987 \pm 0.000008$ (15 ppm, $n = 16$) and $^{143}Nd/^{144}Nd = 0.511922 \pm 0.000052$ (101 ppm, $n = 19$). Samples were diluted at a similar concentration in a 0.05 M HNO_3 solution. The resulting $^{143}Nd/^{144}Nd$ ratios were normalised to the reference value of JNDi-1 $^{143}Nd/^{144}Nd = 0.512115$ (Tanaka et al., 2000).

BHVO-2 and BCR-2 reference materials measured gave $^{143}Nd/^{144}Nd$ normalised isotopic values of 0.512977 ± 0.000006 (11 ppm, n = 3) and 0.512624 ± 0.000004 (8 ppm, n = 2) during session 1, and 0.512969 ± 0.000015 (29 ppm, n = 4) and 0.512636 ± 0.000005 (10 ppm, n = 1) during session 2. Both standards fit within the range of the reference values determined by Weis et al. (2005). Four procedural blanks for Nd were measured as well, obtaining values between 4 and 148 pg (Supplementary table S3).

4. Results

4.1. Bulk rock composition and clay mineral assemblages – XRD analyses

The mineral content of the selected samples was dominated by clay minerals and quartz, accounting together for around 80% of the mineral composition (Supplementary table S4). Other minerals such as K–feldspar and plagioclase were present but in minor proportions, ranging between 15% and 5%. A minor proportion of the samples also contained pyrite, but in quantities lower than 3%. Only three exceptions were found, two samples in which carbonates reached 50% or more (9R6/49–52 and 19R4/99–101), and a third sample (25R1/50–52) where siderite content was 46%.

Smectites dominated the clay assemblages with values ranging between 60% and 98% (Fig. 3; Supplementary table S4). Illite content varied between 5 and 20% throughout the section, while minor proportions of kaolinite, palygorskite, and chlorite were identified with values oscillating between 1% to 13%, 1% to 10%, and <5% respectively (Fig. 3). Two intervals showed depictable variations. First, illite and kaolinite increased by 15 and 8% respectively at the base of the Turonian (ca. 93 Ma). Then, illite and palygorskite increased steadily between the Campanian-Danian interval (ca. 77–66 Ma), and reached a maximum of 20 and 10%, respectively (Fig. 3). Kaolinite and chlorite contents increased marginally as well, although their proportions remained below 5% (Fig. 3).

4.2. Hf – Nd isotopic compositions

The results do not show any significant variations with respect to either of the sample treatment methods performed (i.e., alkaline fusion vs acid digestion) or the column chromatography methods used (i.e., conventional column chromatography vs automated column chromatography using the PrepFAST-MC® – Fig. 3; Table 2). Therefore, we present and discuss the results as a single data set. Hafnium and neodymium isotopic compositions are reported in epsilon notation as the relative deviation from the chondritic reference material (CHUR) reported in Bouvier et al. (2008) with $^{176}Hf/^{177}Hf_{CHUR} = 0.282785$ and $^{143}Nd/^{144}Nd_{CHUR} = 0.512630$:

Table 2
Hf—Nd isotopic compositions. Depth is reported in meters below the sea floor (mbsf). *Ages were calculated using linear interpolations anchored to the tie-points of the age model built from the biostratigraphy intervals reported by Davey (1978) and Bolli et al. (1978). Nomenclature of the samples is as follows, e.g., 9R3/130–132 – core 9, section 3, interval 130–132. Error accounts for the standard error. *ΔεHf was calculated using the clay array correlation: ΔεHf = εHf – (0,78 * εNd + 5,23) published in Bayon et al. (2016). 2σ is the standard deviation calculated for both εNd and εHf. (1) Samples in which the treatment was done by alkaline fusion and the column chromatography extraction was performed only using the PrepFAST-MC®. (2) Sample replicate in which the treatment was done by acid digestion and the column chromatography extraction was done using the PrepFAST-MC®. (3) Sample replicate in which the treatment was done by alkaline fusion and the column chromatography extraction was done using the PrepFast device.

Sample	Depth (mbsf)	Stage	Age (Ma)*	$^{143}Nd/^{144}Nd$	Error	ε_{Nd}	2σ	$^{176}Hf/^{177}Hf$	Error	ε_{Hf}	2σ	$\Delta\varepsilon_{Hf}$*
9R3 / 130–132 (1)	263.80	Thanetian	57.1	0.512164	0.000006	−9.1	0.12	0.282722	0.000006	−2.24	0.2	−0.37
10R4 / 50–52 (1)	274.00	Selandian	59.8	0.512123	0.000007	−9.89	0.13	0.282732	0.000004	−1.88	0.15	0.61
11R2 / 140–142 (1)	281.40	Danian	61.7	0.51209	0.000007	−10.53	0.14	0.282723	0.000005	−2.19	0.19	0.8
11R6 / 100–102 (1)	287.00		63.2	0.512104	0.000006	−10.27	0.12	0.282678	0.000005	−3.77	0.17	−0.99
12R1 / 100–102	298.50		66.1	0.512128	0.000004	−9.79	0.08	0.282708	0.000005	−2.72	0.16	−0.32
12R3 / 99–101	301.40		66.4	0.512137	0.000005	−9.62	0.09	0.282707	0.000004	−2.74	0.14	−0.47
12R3 / 99–101 (2)	301.40		66.4	0.512131	0.000003	−9.73	0.07	0.282717	0.000004	−2.4	0.14	−0.03
12R3 / 99–101 (3)	301.40	Maastrichtian	66.4	0.512136	0.000004	−9.64	0.08	0.282724	0.000004	−2.17	0.18	0.12
12R5 / 50–52	304.00		66.6	0.512133	0.000005	−9.69	0.1	0.282704	0.000004	−2.85	0.15	−0.52
12R5 / 50–52 (2)	304.00		66.6	0.512121	0.000005	−9.92	0.09	0.282713	0.000008	−2.55	0.15	−0.04
12R5 / 50–52 (3)	304.00		66.6	0.512123	0.000004	−9.89	0.07	0.282718	0.000004	−2.37	0.27	0.11
13R1 / 128–130	327.28		68.9	0.512226	0.000004	−7.88	0.08	0.282696	0.000005	−3.16	0.18	−2.25
14R1 / 80–82	364.80		72.5	0.512168	0.000007	−9.01	0.14	0.282678	0.000004	−3.78	0.15	−1.99
14R1 / 80–82 (2)	364.80		72.5	0.512165	0.000004	−9.08	0.08	0.282686	0.000005	−3.5	0.18	−1.65
14R1 / 80–82 (3)	364.80		72.5	0.512163	0.000003	−9.1	0.06	0.28269	0.000002	−3.36	0.08	−1.49
15R1 / 50–52	402.50		76.2	0.512223	0.000004	−7.94	0.08	0.28267	0.000005	−4.06	0.17	−3.1
15R1 / 139–141	402.50		76.	0.512246	0.000004	−7.5	0.09	0.282679	0.000006	−3.75	0.22	−3.13
15R2 / 100–102	403.39		76.4	0.512179	0.000005	−8.79	0.1	0.282673	0.000006	−3.98	0.21	−2.35
16R1 / 129–131	404.50	Campanian	79.9	0.512203	0.000006	−8.33	0.12	0.282671	0.000005	−4.05	0.17	−2.78
16R1 / 129–131 (2)	441.29		79.9	0.512188	0.000003	−8.63	0.07	0.282669	0.000004	−4.11	0.21	−2.61
16R1 / 129–131 (3)	441.29		79.9	0.512188	0.000003	−8.62	0.05	0.282666	0.000006	−4.22	0.14	−2.73
16R6 / 10–12	447.60		80.5	0.512203	0.000006	−8.32	0.12	0.282669	0.000008	−4.09	0.27	−2.83
17R1 / 133–135	479.33		83.5	0.51218	0.000005	−8.77	0.09	0.282656	0.000005	−4.57	0.17	−2.96
17R1 / 133–135 (2)	479.33		83.5	0.512171	0.000003	−8.96	0.07	0.282663	0.000004	−4.32	0.15	−2.56
17R1 / 133–135 (3)	479.33		83.5	0.512172	0.000003	−8.93	0.07	0.282673	0.000004	−3.97	0.13	−2.24
17R2 / 140–142	480.90		83.6	0.51219	0.000005	−8.58	0.1	0.28266	0.000006	−4.41	0.21	−2.94
18R1 / 144–146	526.97	Santonian	85.6	0.512191	0.000004	−8.57	0.08	0.282665	0.000006	−4.25	0.23	−2.8
18R2 / 130–132	528.30		85.7	0.512202	0.000006	−8.36	0.12	0.282661	0.000005	−4.39	0.17	−3.1
19R2 / 70–72	575.20		87.8	0.512185	0.000005	−8.68	0.09	0.282651	0.000003	−4.73	0.11	−3.19
19R4 / 50–52	578.00	Coniacian	87.9	0.512192	0.000005	−8.55	0.09	0.282663	0.000005	−4.33	0.17	−2.89
20R1 / 100–102	611.50		89.4	0.512174	0.000006	−8.9	0.12	0.282645	0.000004	−4.94	0.16	−3.23
20R3 / 70–72	614.20		89.5	0.512213	0.000005	−8.14	0.1	0.282682	0.000005	−3.64	0.18	−2.52
21R3 / 54–56	671.54		90.8	0.512199	0.000006	−8.4	0.12	0.282671	0.000005	−4.05	0.16	−2.72
22R3 / 100–102	719.50	Turonian	91.8	0.512202	0.000005	−8.35	0.1	0.2826656	0.000005	−4.22	0.16	−2.94
23R2 / 120–122	765.70		92.7	0.512216	0.000004	−8.07	0.08	0.282671	0.000004	−4.04	0.15	−2.97
24R4 / 139–141	816.39		93.8	0.512181	0.000004	−8.75	0.08	0.28269	0.000005	−3.38	0.17	−1.78
25R1 / 50–52 (1)	858.50	Cenomanian	99.4	0.512251	0.000006	−7.4	0.11	0.2827219	0.000004	−2.23	0.16	−1.69
25R6 / 100–102 (1)	866.50	Albian	100.5	0.512202	0.000007	−8.35	0.15	0.28269	0.000005	−3.36	0.17	−2.08
26R4 / 50–53 (1)	912.50		107.1	0.51215	0.000007	−9.36	0.14	0.2826926	0.000005	−3.27	0.17	−1.2
27R2 / 53–55 (1)	955.00	Aptian	113.2	0.512255	0.000006	−7.32	0.11	0.2827803	0.000006	−0.17	0.21	0.32

$$\varepsilon_{Hf} = \left(\left[\frac{\left(\frac{176Hf}{177Hf}\right)_{Sample}}{\left(\frac{176Hf}{177Hf}\right)_{CHUR}} - 1 \right] * 10^4 \right) \text{ and } \varepsilon_{Nd} = \left(\left[\frac{\left(\frac{143Nd}{144Nd}\right)_{Sample}}{\left(\frac{143Nd}{144Nd}\right)_{CHUR}} - 1 \right] * 10^4 \right)$$

The measured ε_{Nd} values ranged between −7.3 and − 10.5 ε-units (Fig. 3). Among the section, the data point corresponding to the Aptian with ε_{Nd} of −7.3 was the most radiogenic, while the Albian-Cenomanian interval (ca. 113–93 Ma) showed less radiogenic values that increased from −9.3 to −7.5 (Fig. 3). ε_{Nd} values remained relatively stable along the Turonian–Campanian interval (ca. 93–80 Ma), with values around −8.5, before decreasing during the Campanian–Danian interval (ca. 77–62 Ma) where they reached values around −10, to finally increase up to −9.1 by the end of the Danian (Fig. 3).

The ε_{Hf} values ranged between −4.9 and − 0.2 ε-units (Fig. 3). During the Aptian-Albian (ca. 114–100 Ma) interval the values decreased from −0.2 to −3.2, then stabilized around −3 until a sharp excursion down to −4.9 at the early Coniacian (ca. 89 Ma; Fig. 3). ε_{Hf} values continued steadily around −4.3 from the Coniacian to the Campanian (ca. 89–80 Ma), before an increase up to the Danian (ca. 62 Ma), where they reached up to −2.2 (Fig. 3).

4.3. Major and REE elements

Major oxides concentrations are reported in the supplementary table S5. Most samples are enriched in SiO_2 with concentrations oscillating between 46 and 68 wt%. The CaO wt% content was predominant only in two samples (9R2/50–52 and 19R4/50–52), which is attributable to the presence of carbonate nodules. Second in abundance, were the Al_2O_3 and FeO, with percentages ranging between 8 and 15 wt% and 4 and 10 wt% respectively. Other major oxides like MgO, K_2O, and Na_2O, were present but in minor proportions, with values around 3 wt% or less.

REE abundances within the trace elements for the clay fraction are reported in supplementary table S2. The REE values obtained showed a relatively flat pattern, although a slight enrichment of the medium rare earth elements (MREE) can be depicted when compared to the light and heavy rare earth elements (LREE and HREE respectively; Fig. 4).

4.4. Transmission electron microscopy

Observations performed by TEM analyses on the five selected samples (Supplementary table S1) showed a prevalence of smectite, consistent with the results obtained by XRD. The smectite particles observed exhibited a characteristic flaky-shape texture (Fig. 5A).

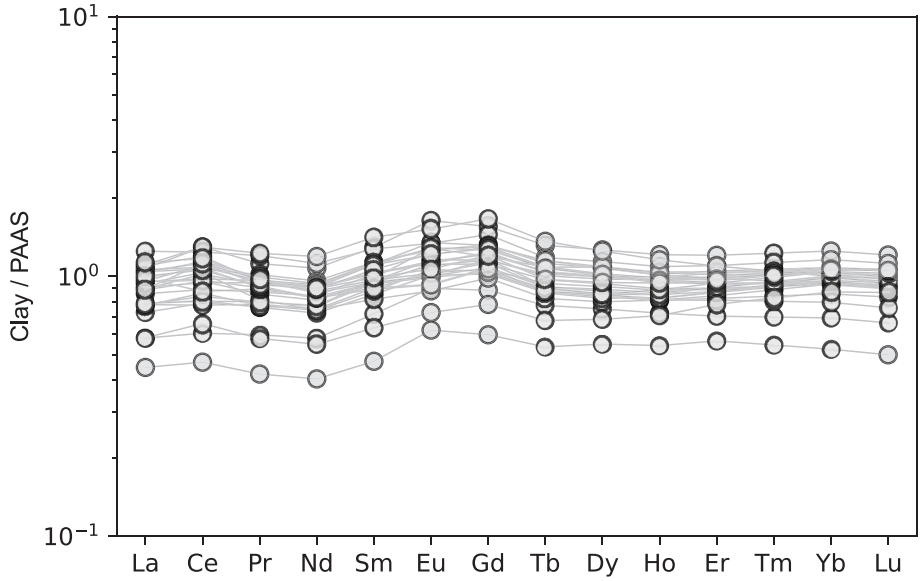

Fig. 4. REE patterns of the clay fraction of the samples analysed for Hf—Nd isotopic compositions. REE contents were normalised to the Post-Archean average Australian Shale (PAAS; Taylor and McLennan, 1985).

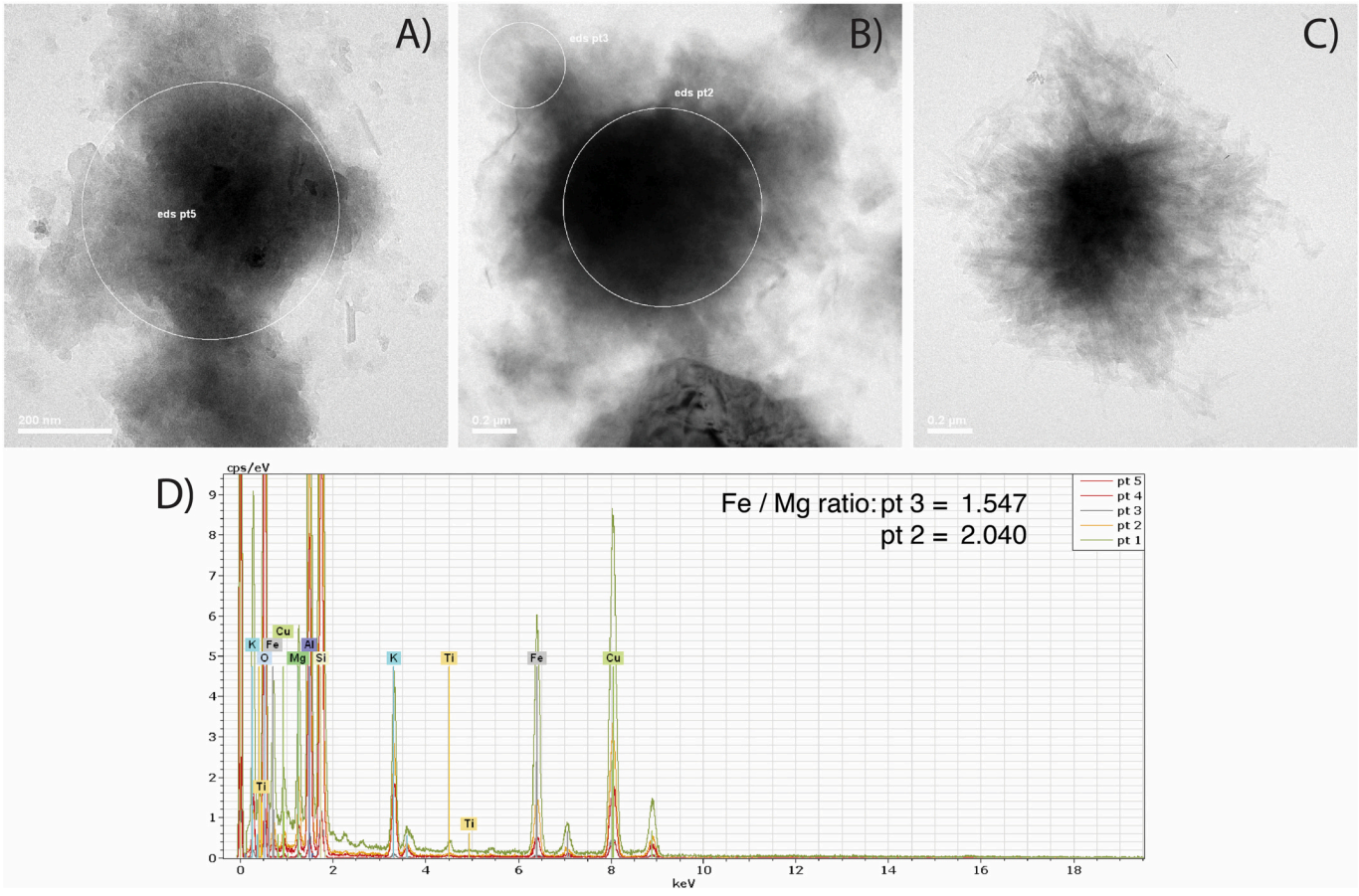

Fig. 5. A) TEM image from sample 11R1 98–100 illustrating the flaky-shape texture observed in most of the smectite crystals. B) TEM image taken from sample 17R2 140–142 showing a smectite particle and the transition from a flaky-shape texture to lath-shaped regrowth. Five chemical measurements (pt1-pt5) were carried out on this particle, from centre outwards. C) TEM image from sample 15R2 139–141 showing a smectite crystal with lath-shaped regrowths on the edges. D) Spectra profile showing the measurements performed on sample 17R2 140–142, the more relevant are pt2 and pt3 as they were calculated in the areas showing the transition in textures, ratios show the Mg increase outwards.

Although a majority of smectite particles displayed such texture, some exhibited evidence of lath-shaped habit with intermediate patterns (Fig. 5B and C). Some particles probably represent a mixture of fibrous clay (i.e., palygorskite) and smectite, likely related to transformation of inherited smectite into palygorskite or illite (Fig. 5B and C). Chemical analyses performed on some of these lath-shaped and intermediary structured particles showed variations in Fe—Mg content, illustrating an outwards increase in Mg compared to Fe (Fig. 5B and D).

Illite and palygorskite were found in minor proportions. Illite particles were observed mostly as regular-edged crystals with occasional dented borders (Fig. 6A). Palygorskite particles showed thin fibrous morphology (Fig. 6B), especially in samples from the upper part of the section, in agreement with XRD analyses.

5. Discussion

5.1. Sediments nature and sources

Variations in clay mineralogy and geochemical composition along the DSDP core 361 may provide insights into the timing and evolution of denudation processes in the South African Plateau. However, to interpret clays as product of surface continental processes, they should have a detrital origin (e.g., Adatte et al., 2000; Bougeault et al., 2017; John et al., 2012; Kemp et al., 2016). In marine environments, authigenic clays can form during early diagenesis, resulting in a partial imprinting of seawater signal in the clay assemblages, whereas burial diagenesis can modify the primary signal through the transformation of clay minerals. As such, to interpret the clay mineralogical changes as variations of surface continental processes it is imperative that these are of detrital origin and not affected by significant authigenesis or burial diagenesis.

TEM analyses showed a large preponderance of Al—Fe smectites with flake-like textures, indicating a predominant detrital nature of the clays at the studied site (Fig. 5 - Chamley, 1989; Clauer, 1990; Fagel et al., 2001). This is consistent with the textures observed for the illite and palygorskite, which did not show regrowths or euhedral morphologies typical of authigenic processes (Fig. 6). The short and slim broken morphologies of palygorskite crystals indicate long transport (i.e., at least the length of a small catchment) and reworking, either from confined and shallow continental waters or peri-marine environments (Chamley, 1989; Knidiri et al., 2014; Thiry and Pletsch, 2011). Likewise, the regular slightly dented illite crystals are typical of detrital origin (Fig. 6A; Chamley, 1989). Scarce smectite particles with high Mg-content and regrowth patterns at the fringe were nonetheless observed (e.g., sample 15R2 139–141 – Fig. 5C). This suggests smectite transformation into fibrous post-depositional clay minerals such as illite-smectite mixed layers or to a minor extent into fibrous clay (i.e., palygorskite), caused by early diagenetic processes, which is common in deep marine environments with low terrigenous input (Knidiri et al., 2014; Pletsch, 2001; Setti et al., 2004). However, the scarcity of these features along with the short and broken morphologies of palygorskite crystals suggests a minor influence of these early diagenetic processes on clay assemblages. This is further supported by REE analyses that corroborate the predominantly detrital nature of the studied clay assemblages. The REE patterns observed did not show either Ce anomalies or HREE enrichment, typical features of authigenic clay formation in marine environments (Bayon et al., 2015; Fagel et al., 1992; Laveuf et al., 2012). Likewise, no evidence of burial diagenesis such as smectite illitization was observed (Lanson et al., 2009; Nadeau et al., 1985), indicating that there is not a significant imprint of seawater signal or burial diagenesis in the clays at DSDP core 361, that we consider as reflecting mainly sediments of detrital origin.

Paleodrainage studies have suggested that during the late Cretaceous (ca. 113–66 Ma) there were two river systems (Karoo and Kalahari; Fig. 11) draining out of the western Southern African coast, however these eventually merged into the modern Orange river system by the early Cenozoic (ca. 60 Ma) (De Wit et al., 2009; De Wit, 1999; Goudie, 2005). The outlet of the Karoo paleo-river has been identified south of the current Orange river, likely close to the modern Olifants river outlet. This implies that the Karoo paleoriver was likely the main source of sediments transported into the Cape Basin during the late Cretaceous (93.9–66 Ma), and that the source-to-sink system of the Cape Basin comprised potentially a larger catchment when compared to the modern Olifants river system, that could have included areas as far as the central part of the South African Plateau.

Neodymium isotopic compositions of sediments have been widely used to track sediment sources in marine basins. This is based on the

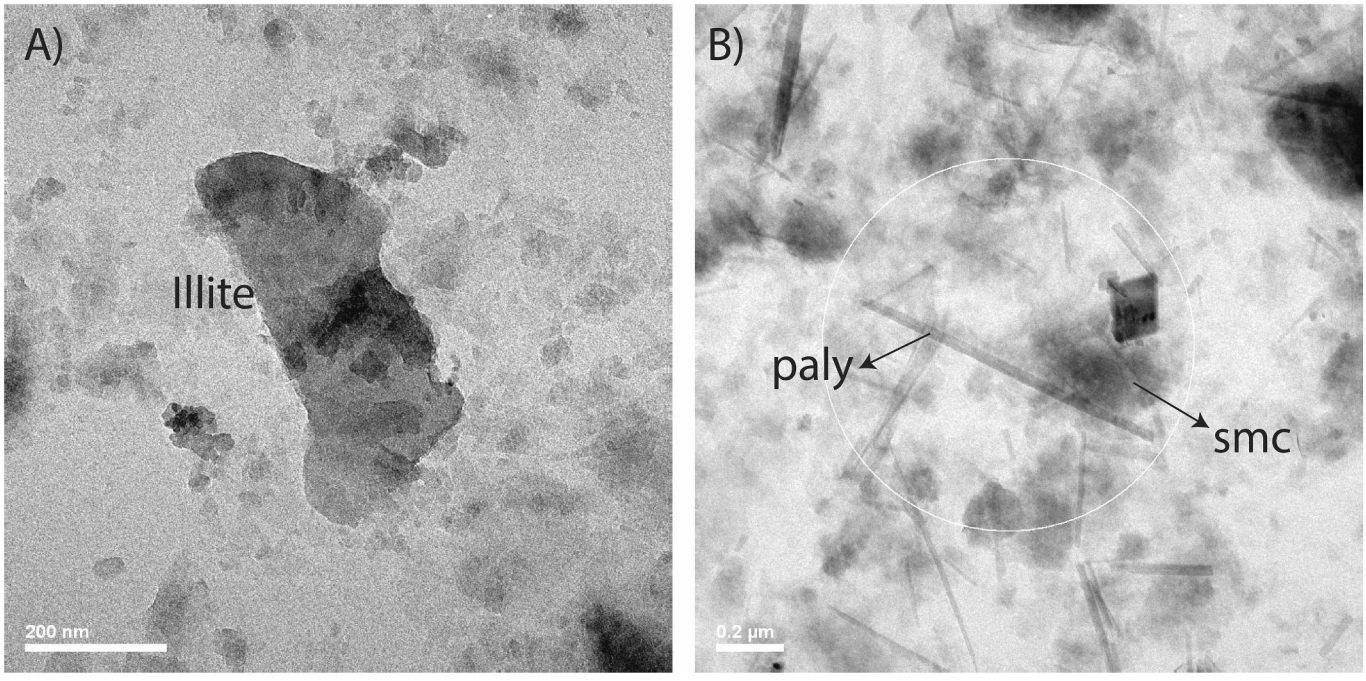

Fig. 6. A) TEM image from sample 11R1 98–100 showing an illite particle with regular- shaped borders, the border on the right of the crystal exhibits some dents. B) TEM image from sample 13R1 52–54 displaying fibrous palygorskite (paly) over a flaky-shaped smectite particle (smc).

principle that Sm—Nd ratios remain unfractionated during surface continental processes (Frank, 2002; Goldstein and Hemming, 2003; Jeandel et al., 2007). Comparison of ε_{Nd} values of the sediments deposited at site 361 with the values of the main units on the South African Plateau may thus bring some further insights on the source areas drained to the Cape Basin during the late Cretaceous (93.9–66 Ma). A compilation of ε_{Nd} data for those units (Fig. 7; supplementary table S6) shows a predominance of very unradiogenic values at the eastern margin, typical of old crustal greenbelt rocks represented by the Kaapvaal craton (mean $\varepsilon_{Nd} = -37$). On the western margin, the succession of metasedimentary and volcanic rocks from the Namaqua belt (2.5–1.6 Ga), and the low-grade metasediments of the Cape Belt (546–251 Ma), both display mean ε_{Nd} values around −16 and − 11. The Saldania Belt in contrast yields more radiogenic values (mean $\varepsilon_{Nd} = -6$), attributed to the presence of Cambrian (~540 Ma) granitic intrusions. In the central area, both Karoo and Kalahari sediments encompass different deposition cycles and thus, different sediment sources (Catuneanu et al., 2005; Garzanti et al., 2022; Vainer et al., 2018). Mean values for the Karoo sequences are around −10, likely representing a mixture between the multiple sedimentary sources mentioned above and the highly radiogenic Karoo flood-basalts (mean $\varepsilon_{Nd} = -3.7$). Kalahari sequences have been deposited since late Cretaceous (~88 Ma), initially through fluvial deposition, and then through aeolian processes from the Pliocene onwards (Haddon and McCarthy, 2005). Although some ε_{Nd} data (Garzanti et al., 2014; mean = −36) favor cratonic rocks as mains sources, more in-depth provenance analyses have shown several recycling cycles of the surrounding geological units, including the Karoo basalts (Garzanti et al., 2022).

The ε_{Nd} values measured on the clay fraction of sediments from DSDP core 361 (between −7.3 and − 10.5 ε-units) exclude major source changes in the detrital material deposited during the late Cretaceous (93.9–66 Ma) (Fig. 3). Such values are consistent with a main source located on the western-central and western-south areas of the South African plateau, which could be either the Karoo sediments, and/or a mixture of volcanic and metasedimentary sequences of the Cape, Saldania, and Namaqua belts that constitute the Southern-west African margin. However, the decrease in the ε_{Nd} values from −8 to −10 depicted between the Campanian-Danian (77–62 Ma) interval, suggests an increase in sediment input of more unradiogenic sources, which could arise from a larger contribution of the western Cape and/or Namaqua belts (Fig. 7).

Some studies have reported the presence of deep-ocean currents during the late Cretaceous (93.9–66 Ma) (e.g., Dummann et al., 2020; Murphy and Thomas, 2013; Natland, 1978), suggesting a scenario where sediments from the conjugate Argentinian basin, the Antarctic, and even the Indian Ocean could have been brought to the Cape Basin. It is unclear their extent and impact, and more in-depth studies assessing the direction and potential sediment transport by these bottom currents are still needed. Nevertheless, even if such currents have had an impact in the sediment sources, still our ε_{Nd} data, the drainage configuration analyses (De Wit et al., 2009; De Wit, 1999; Goudie, 2005), and the palynological studies (Sandersen, 2006), show strong evidence supporting a predominant sediment source from the west-south and central-south part of the South African Plateau to the Cape Basin.

5.2. Evolution of physical erosion

Variations in detrital clay mineral assemblages have been widely used to infer changes in hydrolysing conditions and physical erosion affecting source rocks (e.g., Chamley, 1989; Chenot et al., 2018; Dera et al., 2009; Kemp et al., 2016; Ruffell et al., 2002; Thiry, 2000). Illite and chlorite can be considered as primary clay minerals as they are produced from various types of rocks under limited chemical weathering conditions and quick remobilization by physical erosion (Chamley, 1989). They are typically observed in dry-cold environments, or in active tectonic settings where physical erosion predominates among denudation processes (Chamley, 1989). In contrast, smectites are formed during pedogenesis under more intense weathering of silicate minerals, typically in semiarid to temperate-humid seasonally contrasted climates (Chamley, 1989; Ruffell et al., 2002). Kaolinite is

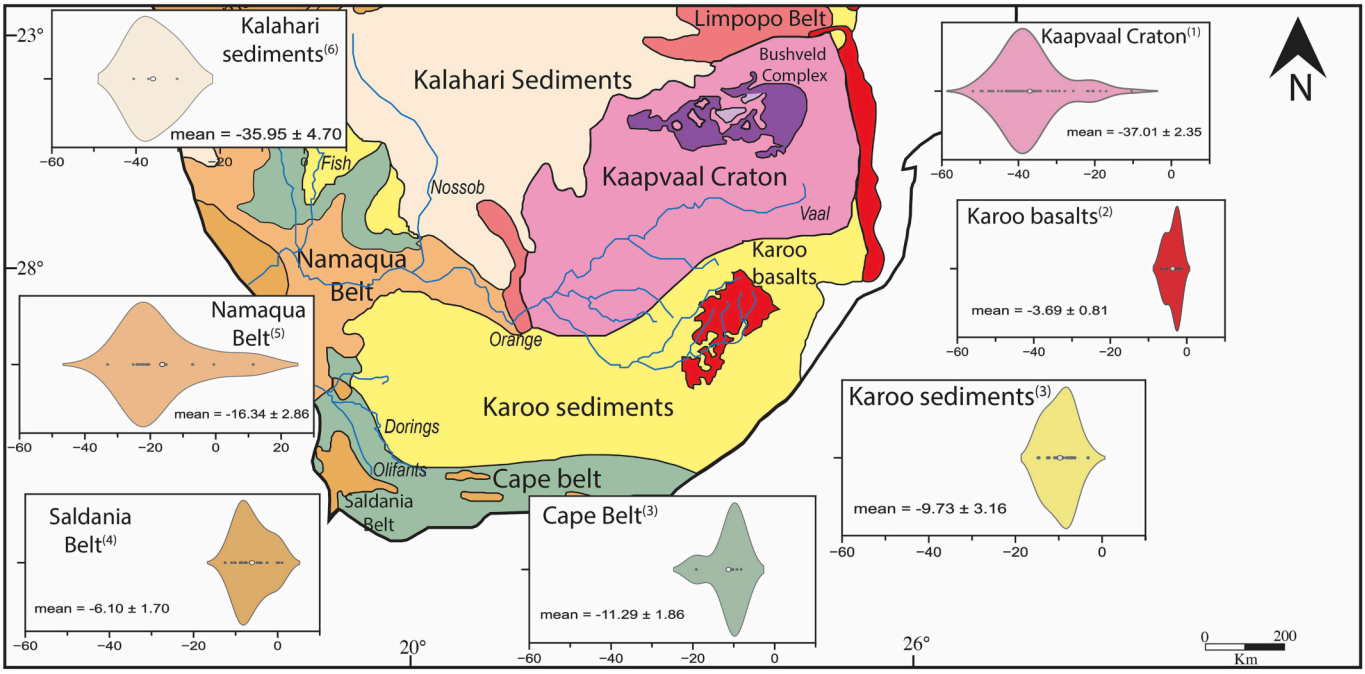

Fig. 7. Compilation map of mean present-day ε_{Nd} values for the main source units of Southern Africa. Modified after Garzanti et al. (2014). There are large variations within each unit because they consist of multiple lithologies, therefore we added violin plots (white circle displays the position of the mean value) to display the distribution of the data. The data are compiled as follows 1) Kaapvaal craton (Schoene et al., 2009); 2) Karoo basalts (Hawkesworth et al., 1984); 3) Karoo sediments and Cape belt (Dia et al., 1990); 4) Saldania belt (Chemale et al., 2011); 5) Namaqua belt (Reid, 1997); 6) Kalahari sediments (Garzanti et al., 2014). Supplementary table S6.

formed under highly hydrolysing conditions, commonly observed in tropical environments with very active drainages (Chamley, 1989; Thiry, 2000), whereas palygorskite is formed under arid or semi-arid conditions, in continental or peri-marine environments subject to pronounced evaporation (Chamley, 1989; Knidiri et al., 2014; Pletsch et al., 1996). Therefore, in active tectonic episodes, the relative abundance of primary clay minerals expressed by the Illite + Chlorite / Smectite (I + C/S) ratio can provide insights regarding the evolution of physical erosion on continental settings (e.g., Corentin et al., 2022, 2023; Kemp et al., 2016).

At DSDP core 361, clay mineral assemblages are largely dominated by smectite, accounting for about 80% of the total clay content. Such feature is commonly observed in marine environments during the Cretaceous, and widely interpreted as a consequence of the formation of contemporaneous soils (Chamley, 1981; Corentin et al., 2022, 2023; Robert, 1987). This predominance is observed in the evolution of the (I + C)/S ratio (Fig. 8), however there are two considerable changes in the clay assemblages (Fig. 3). First, an increase in both illite (15%) and kaolinite (8%) is observed during the Turonian (93 Ma). This increase in clay minerals that form in very different environments is better explained by sediment reworking leading to the transport and deposition of detrital clays that are not contemporaneous of climate conditions forming soils. The second change is an increase in primary clay minerals, starting at the Campanian (ca. 77 Ma) and reaching a maximum during the Danian (ca. 62 Ma), before decreasing again around the Danian-Selandian boundary (ca. 61 Ma). This increase is mainly characterized by illite, although an increase in palygorskite, and a minor variation in kaolinite are also observed (<5%) (Fig. 3). Such increase in illlite suggest an enhancement of physical erosion during the Campanian-Danian interval, which is also supported by an increase in sedimentation rates recorded in the Cape Basin during the Campanian-Maastrichtian (Fig. 8; Baby et al., 2019). The concomitant decrease in ε_{Nd} values, although moderate, reflects a change in the source material eroded. These changes might be linked either to an increase in contribution from already present unradiogenic rocks, or a new source's input of unradiogenic rocks potentially brought by enhanced denudation or by a change in the drainage configuration, linked to the uplift episodes of the Southwestern African margin (e.g., Braun et al., 2014; Stanley et al., 2021).

5.3. *Evolution of silicate chemical weathering: Hf – Nd isotopic compositions of the clay fractions*

The depicted changes in clay mineralogical assemblages suggest an increase in physical erosion during the Campanian–Danian interval. Physical erosion can enhance silicate chemical weathering by disaggregation of exposed rocks and continual exposure of fresh material to weathering processes. There is however a threshold to this correlation

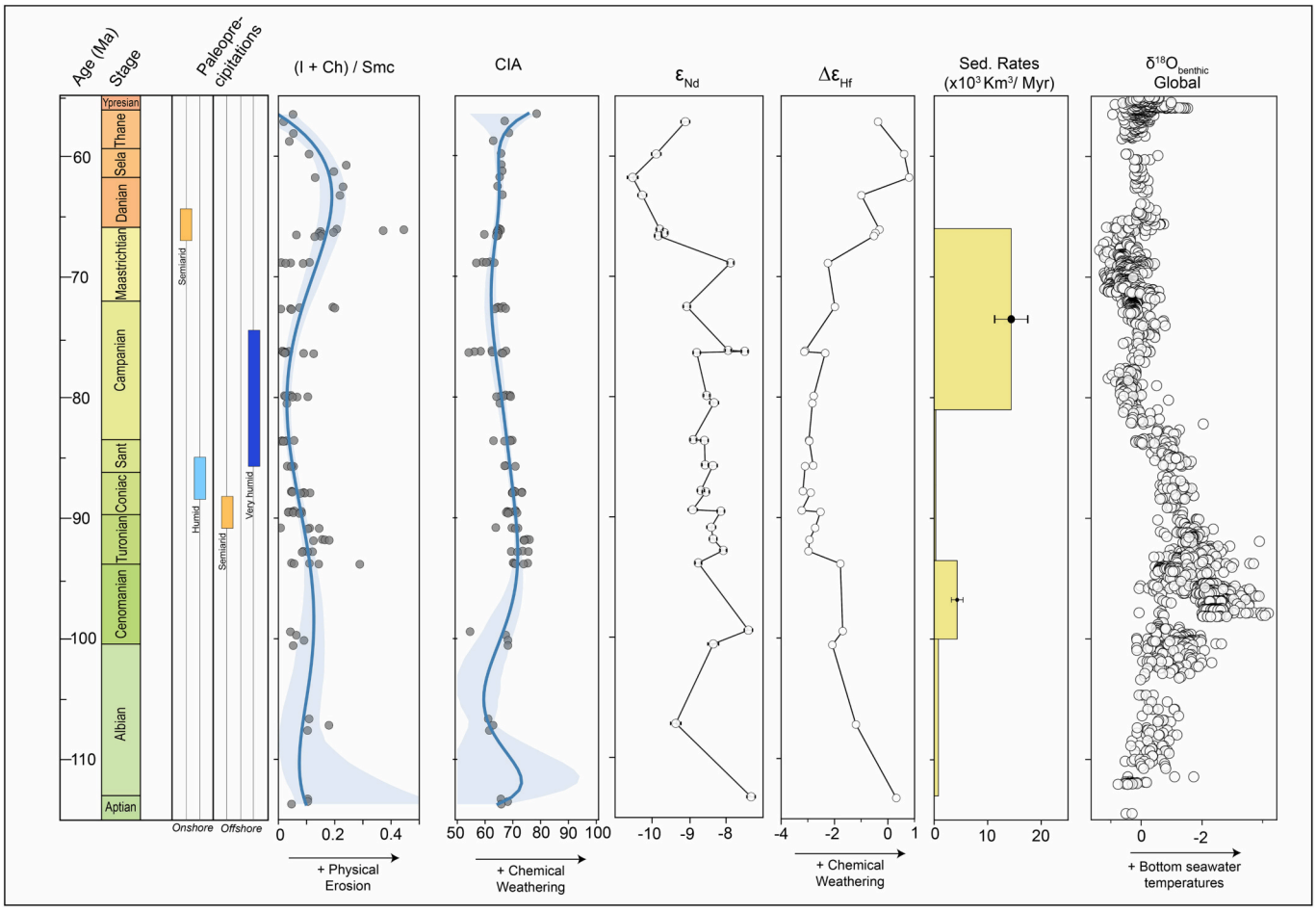

Fig. 8. Illite + Chlorite / Smectite (I + C/Smc) ratio, Chemical Index of Alteration (CIA), ε_{Nd}, $\Delta\varepsilon_{Hf}$, from units 5 and 6 of DSDP site 361. Palaeoprecipitations of the South African plateau are based on palynology data set compiled in Braun et al. (2014). Dataset: Bamford and de Wit (1993); Bamford and Stevenson (2002); Rayner et al. (1997); Sandersen (2006); and Smith (1988, 1986). Sedimentation rates of the Cape Basin are estimations calculated by Baby et al. (2019). $\delta^{18}O$ records in global benthic foraminifera are from Friedrich et al. (2012); including data from Zachos et al. (2008) for the Cenozoic. Samples with replicates in ε_{Nd} and $\Delta\varepsilon_{Hf}$ values were averaged, and the mean was used to plot the curve. Smoothed curves with their 95% confidence interval have been calculated using Kernel regressions for (I + Chl)/Sm, and CIA ratios.

where remobilization caused by physical erosion occurs too fast for the material to be extensively weathered (kinetically-limited regime - Gabet and Mudd, 2009). Consequently, the correlation between silicate chemical weathering and physical erosion is not straightforward, especially in active tectonic settings which are commonly linked to high erosional rates (e.g., Louvat and Allègre, 1997; Millot et al., 2002).

Multiple indices comparing mobile to immobile major elements have been used to track changes in silicate chemical weathering (e.g., the Weathering Index of Parker (WIP; Parker, 1970) or the Continental Weathering Index (CIW; Harnois, 1988). Here we calculated the most widely used Continental Index of Alteration (CIA - Fig. 8; Nesbitt and Young, 1982). Calculated CIA values (Supplementary table S5) oscillated between 65 and 80 but stayed predominantly around 70. Although some variations can be depicted in the data, particularly at the Aptian–Albian interval (113–100 Ma) and during the Thanetian (58 Ma), the index remained rather stable with only a subtle long decrease during the Turonian-Campanian interval. This steadiness would indicate no major changes in chemical weathering during the late Cretaceous, in spite the reported climate variations and tectonic activity. However, the distal location of the DSDP core 361 (abyssal plain) and deposition of the sediments under the CCD, are factors that likely influenced the content of major oxides. In particular, Al_2O_3, enriched on clay minerals, and CaO, perturbed under the CCD. Therefore, the CIA index does seem to represent a reliable approach to track changes in silicate chemical weathering, at least in sediments deposited in deep environments.

To understand variations in silicate chemical weathering and explore its response to changes in physical erosion, we used then the combined isotopic systems of Sm—Nd and Lu—Hf on clay fractions. This proxy was developed in modern environments, and has also been successfully applied to ancient environments (Bayon et al., 2012; Corentin et al., 2022, 2023). These isotopic systems behave similarly during magmatic processes, and such correlation can be observed through the tendency called the terrestrial array (Fig. 9A; Vervoort et al., 2011). However, during surface continental processes these systems decouple. A large part of this decoupling arises from mineral sorting during transport from source areas to the basin, resulting in higher ε_{Hf} values on the clay fraction, which is depleted in unradiogenic zircons when compared to coarser fractions (Carpentier et al., 2014; Chauvel et al., 2014; Garçon et al., 2013, 2014; Patchett et al., 1984; Vervoort et al., 2011). Zircons are characterized by a very unradiogenic signature (i.e., low ε_{Hf}) and high concentrations in Hf. Thus, when present, they dominate the Hf budget on detrital sediments. Clay fractions display a distinct εHf-εNd correlation called the clay array (Fig. 9B; Bayon et al., 2016). As such, and due to preferential release of radiogenic Hf associated to mineral phases easily weatherable and Lu-enriched (Bayon et al., 2006), the offsets of εHf from this clay array defined as ΔεHf can be linked (in significant proportion) to silicate chemical weathering.

The clay fractions analysed at DSDP core 361 shows low Zr concentrations, ranging from 81 to 203 ppm (Fig. 10; supplementary material S2), and laying in the clay-sized 'zircon-free' array (Bayon et al., 2016). Importantly, no correlation is observed between Zr concentrations and both ε_{Hf} and $\Delta\varepsilon_{Hf}$ (Fig. 10), excluding a control of the isotopic signal by zircon abundance in the analysed clay fraction. This suggests that variations in $\Delta\varepsilon_{Hf}$ can be linked to changes in the intensity of silicate chemical weathering in the South African margin. Our new $\Delta\varepsilon_{Hf}$ data shows an increase in silicate chemical weathering during the Campanian-Danian interval (77–62 Ma; Fig. 8). Based on εNd isotope data and paleodrainage studies (De Wit et al., 2009; De Wit, 1999; Goudie, 2005), such enhancement may have affected a region extending from the south-western to south-central part of the South African Plateau. More importantly, our new data depict for the first time the existence of important changes in chemical weathering in the South African Plateau during the late Cretaceous.

It could be noted though that low $\Delta\varepsilon_{Hf}$ values (around − 3) are observed during the Turonian, which despite the cooling onset is still a warm period, whereas such low values are recorded at present environments in cold dry climatic zones (Bayon et al., 2016). The relationship between absolute $\Delta\varepsilon_{Hf}$ values with climatic parameters such as mean annual temperature (MAT) or mean annual precipitation (MAP) used to define climate zones may vary between our present-day icehouse period, with its low CO_2 levels and permanent polar icesheets, and the greenhouse climate of the Cretaceous, characterized by markedly higher CO_2 levels and mostly absence of permanent polar icesheets. Such different climate states may result in a quite different hydrological cycle and different relations between climatic parameters, weathering, and absolute $\Delta\varepsilon_{Hf}$ values. As a result, we limit our interpretation to relative changes in $\Delta\varepsilon_{Hf}$ values rather than interpreting absolute $\Delta\varepsilon_{Hf}$ values. Regardless this limitation, our data emphasise the relevance of this new $\Delta\varepsilon_{Hf}$ proxy over traditional indices to track changes in silicate chemical weathering in ancient environments, and in this case, especially in sediments deposited in deep marine environments.Source-to-sink analysis: Tectonic vs climatic forcing and signal propagation

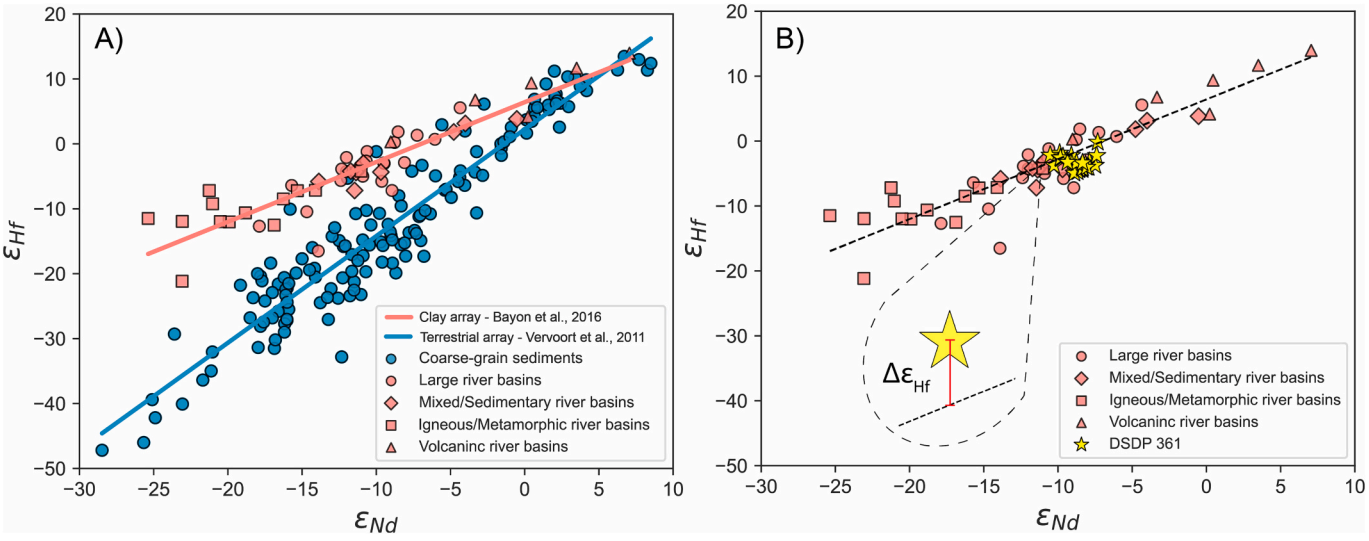

Fig. 9. A) Compilation of εHf and εNd values used to interpolate the terrestrial array (Vervoort et al., 2011) and the clay-fraction array (Bayon et al., 2016). Modified from Bayon et al. (2016) B) Data from DSDP site 361 compared to the εHf-εNd values of the clay array. Zoom-in illustrates the $\Delta\varepsilon_{Hf}$ graphically. Modified from Bayon et al. (2016).

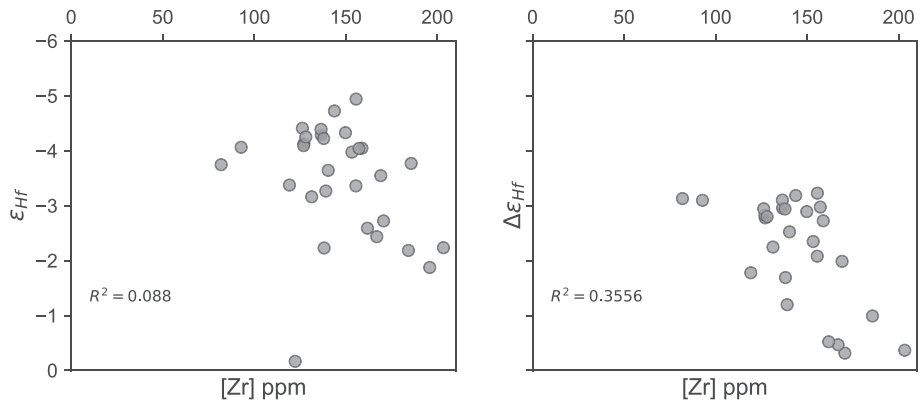

Fig. 10. ε_{Hf} vs Zr (in ppm) and $\Delta\varepsilon_{Hf}$ vs Zr (in ppm). Zr content is assumed as an indicator of the presence of zircon. The R^2 coefficient for both graphs shows low correlation between the values.

5.4. Source-to-sink analysis: Tectonic vs climatic forcing and signal propagation

Clay mineral assemblages and $\Delta\varepsilon_{Hf}$ variations point to a concomitant increase in both physical erosion and silicate chemical weathering in the South African plateau during the Campanian – Danian interval (ca. 77–62). This positive correlation is consistent with the observations of modern environments under supply-limited conditions (Gabet and Mudd, 2009).

Both, tectonics through relief reorganisation, and climate through changes in precipitation and temperature might have an impact on physical erosion and silicate chemical weathering processes over long timescales (Burbank and Anderson, 2012; Romans et al., 2016). Benthic foraminifera $\delta^{18}O$ records (Fig. 8; Friedrich et al., 2012) evidence a long term global cooling trend during the late Cretaceous, which is also supported by planktonic foraminifera and Tex86 data at different latitudes (O'Brien et al., 2017), especially during the Turonian-Campanian interval (ca. 93–80 Ma). Paleoclimatic data in the studied area are quite scarce and relies mainly on palaeoflora data sets. Based on the compilation by Braun et al. (2014), the paleoflora data from onshore sites; although localized and from sites relatively far apart from each other, suggest an evolution from humid to semi-arid climate on inner areas of the South African Plateau during the Turonian-Danian interval (ca. 93–66 Ma) (Fig. 8; Braun et al., 2014). This inland aridification is further supported by the increase of around 10% in palygorskite observed in clay mineralogical assemblages at site 361 during the Campanian–Danian interval (ca. 77–62 Ma), which is a paleoenvironmental indicator of arid to semiarid conditions (Chamley, 1989; Knidiri et al., 2014; Pletsch et al., 1996). Cooler and arid conditions tend to hamper denudation processes. Thus, it seems unlikely that either global and/or regional climate changes acted as the main drivers of the recorded increase in denudation processes.

Multiple thermochronology studies (AFT and AHe) have established thermal models inferring rock cooling periods during the late Cretaceous in the South African Plateau, such periods have been interpreted as enhanced denudation along the South African Plateau, although at different areas and with multiple regional controls over a period ranging from 115 to 60 Ma (Raab et al., 2002; Wildman et al., 2015, 2016; Kounov et al., 2009, 2013; Tinker et al., 2008; Green et al., 2017). These episodes of rock cooling interpreted as episodes of enhanced denudation have been largely attributed to tectonic activity generating continental uplift, partly controlled by regional structures (e.g., Kounov et al., 2009; Raab et al., 2002; Stanley and Flowers, 2020; Tinker et al., 2008; Wildman et al., 2015, 2016, 2021). Most of the AFTA data from the southern margin and the southernmost western margin predominantly shows rock cooling initiating in the middle Cretaceous (ca. 110 Ma) and extending up to the Campanian-Maastrichtian (ca. 75 Ma) (Fig. 11, Wildman et al., 2015, 2016; Kounov et al., 2009; Tinker et al., 2008). This period mostly predates the marked increase in physical erosion and chemical weathering inferred from our data set in the Cape Basin, although in its later stages it overlaps with the increase in I + C/S ratio and $\Delta\varepsilon_{Hf}$ (Fig. 11). This time lag is unlikely linked to uncertainties in the site 361 age model, as the Santonian-Maastrichtian and Maastrichtian-Danian boundaries are relatively well defined. It may arise from the response time required for clays to be eroded after their formation during pedogenetic processes in soils and their transport into the Cape Basin, as it has been previously suggested by some authors that described gaps that could be higher than 1 Myr (Price et al., 2005; Thiry, 2000). Alternatively, tectonic uplift that is thought to have leaded to rock cooling episodes and increased erosion rates, evidenced by AFTA data, could have induced changes in drainage patterns and sediment routing systems (i.e., De Wit et al., 2009; De Wit, 1999; Goudie, 2005), leading to shifts in depocenter in the adjacent marine basins.

Thermochronological studies conducted on the south-western central area of the Plateau show predominant cooling in thecentral part of the Plateau around the 115–90 Ma interval (e.g., Kounov et al., 2009; Stanley et al., 2013; Wildman et al., 2016; Fig. 11), whereas data from the most western areas show cooling extending up to ca. 80 Ma (Wildman et al., 2015). These episodes of rock cooling highlighting periods of enhanced denudation point to an uplift beginning in the central-western areas as early as the mid-Cretaceous (ca. 100 Ma), that as stated above is not recorded in our data nor in the evolution of sedimentation rates in the Cape Basin available in the literature (Fig. 11; Baby et al., 2019). Most likely the Kalahari River (i.e., paleo-orange river; De Wit et al., 2009; De Wit, 1999; Goudie, 2005) was the main drainage system in the western central area, and it was feeding almost exclusively the Orange Basin, which is supported by the large sedimentation rates observed in the Orange Basin between 93.5 and 81 Ma ($51.4 \times 10^3 \pm 11$ Km^3/Myr; Baby et al., 2019), while low sedimentation rates are recorded in the Cape and Outeniqua Basins at this period ($0.3 \times 10^3 \pm 0.06$ Km^3/Myr and $1.3 \times 10^3 \pm 0.3$ Km^3/Myr, respectively; Baby et al., 2019). Thermochronological data from more southern areas (Green et al., 2017) evidence cooling ages between 85 and 75 Ma, overlapping the denudation episode suggested by our data and by the higher sedimentation rates in the Cape Basin (81–66 Ma;$14.4 \times 10^3 \pm 3.1$ Km^3/Myr) (Fig. 11; Baby et al., 2019), although still initiating earlier. It is possible that sediments deposited in the Cape Basin partly come from the southernmost areas, potentially from the Cape Belt and transported by the Karoo paleoriver (Fig. 11). This would be also consistent with the observed shift to more unradiogenic values in the ε_{Nd} data during the Campanian-Danian (ca. 77–62 Ma).

Based on a modelling approach coupled with variations in volumes and sedimentation rates of the basins along the South African margin (Braun et al., 2014; Baby et al., 2019; Stanley et al., 2021), continental tilting has been suggested as a relevant aspect of the tectonic activity during the late Cretaceous. These studies have suggested an initial uplift

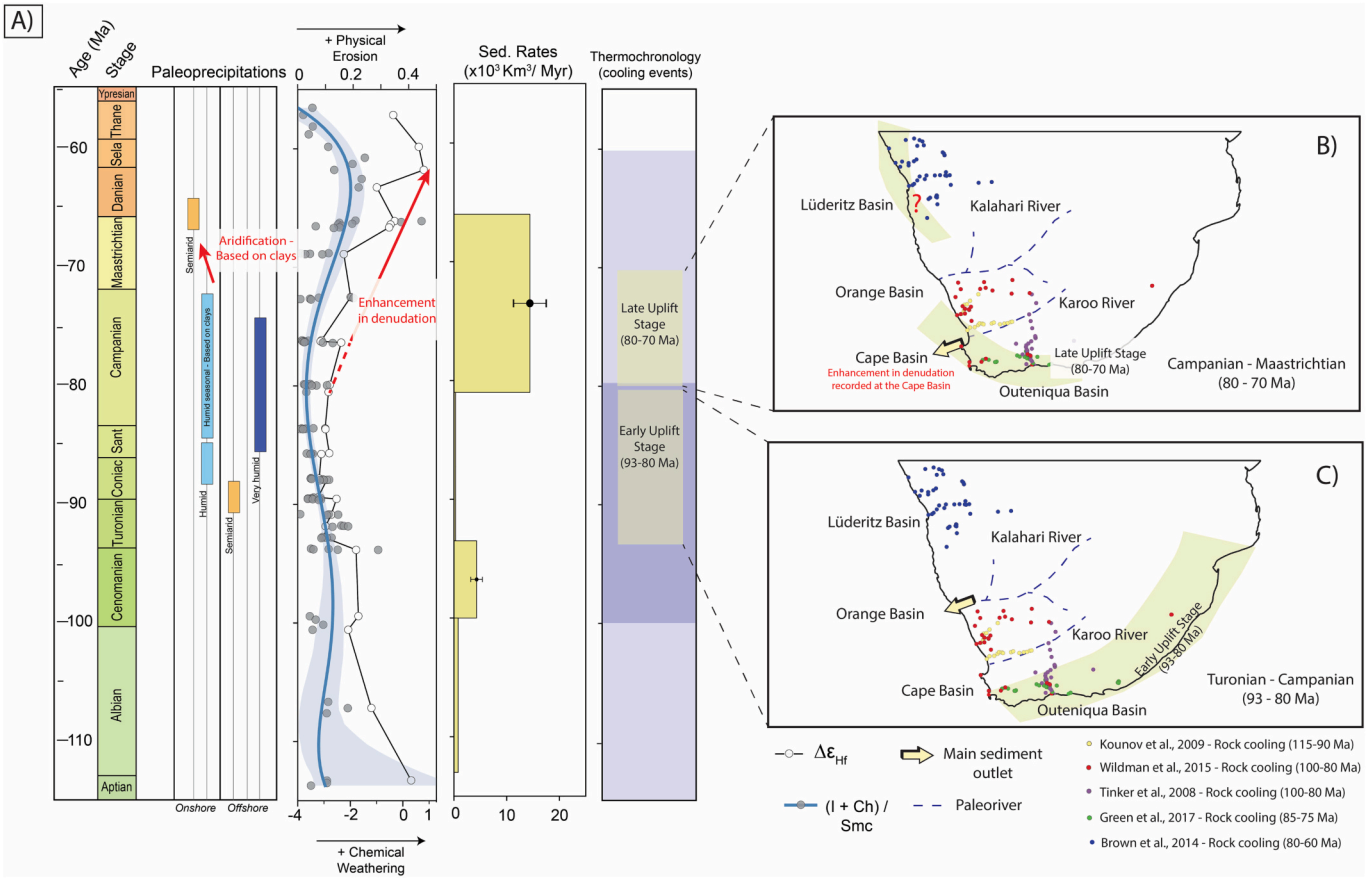

Fig. 11. A) Palaeoprecipitations, Illite + Chlorite / Smectite ratio (I + C/Smc), $\Delta\varepsilon_{Hf}$, sedimentation rates of the Cape Basin, and rock cooling events reported by Thermochronology. Paleoprecipitations are based on palynology data sets compiled by Braun et al. (2014) (Dataset: Bamford and de Wit, 1993; Bamford and Stevenson, 2002; Rayner et al., 1997; Sandersen, 2006; Smith, 1986, 1988). Sedimentation rates of the Cape Basin are estimations done by Baby et al. (2019). Purple box represent the intervals reported of rock cooling by Brown et al. (2014); Green et al. (2017); Kounov et al. (2009); Tinker et al. (2008); and Wildman et al. (2015). The darkest purple part indicate the most common period while the lighter indicates extended periods reported by Brown et al. (2014); Kounov et al. (2009). Uplift stages are proposed by Baby et al., 2019. B) South African setting during the late uplift stage (80–70 Ma) where uplift is suggested both at the southern and northern western areas (Brown et al., 2014; Green et al., 2017) of the Plateau. The Cape Basin is the main depocenter at this period and records the enhanced physical erosion and chemical weathering at the time. Despite the cooling interval reported by Brown et al. (2014) the sedimentation rates remain low in both the Lüderitz and Orange Basins C) South African setting during the early uplift stage (93–80 Ma) where uplift is suggested in eastern areas of the Plateau, but thermochronology suggest potential cooling episodes in central areas too (Tinker et al., 2008; Wildman et al., 2015). The Orange Basin is the main depocenter at this period and the Cape Basin does not seem to record the changes from onshore. B) and C) modified after Baby et al., 2019. (For interpretation of the references to colour in this figure legend, the reader is referred to the web version of this article.)

stage along the eastern margin of Southern Africa between the Turonian-Campanian interval (ca. 93–80 Ma), and a second stage along the western margin during the Campanian-Maastrichtian interval (ca. 80–70 Ma) (Fig. 11; Baby et al., 2019). Importantly, such stages are associated to the increases in sediment deposition in the basins located along the margin. During the first stage (93–80 Ma), sedimentation rates increase in the basins located on the eastern margin (i.e., Walvis, Lüderitz, and Orange), while during the second stage (80–70 Ma) they increase in the basins located on the south-eastern and western margin (i.e., Cape, Outeniqua, Transkei, Durban) (Fig. 11; Baby et al., 2019; Guillocheau et al., 2012; Rouby et al., 2009). In the Cape Basin, the main episode of sedimentation rates increase occurs during the Campanian-Maastrichtian interval (81–66 Ma) and it is linked to the second uplift stage (Fig. 11; $14.4 \times 10^3 \pm 3.1$ Km^3/Myr; Baby et al., 2019), which is coherent with the episode of enhanced denudation inferred from our I + C/S and $\Delta\varepsilon_{Hf}$ data. No major change in denudation processes is observed in our data set during the period of low sedimentation rates of the Cape Basin (93–81 Ma; $0.3 \times 10^3 \pm 0.06$ Km^3/Myr; Baby et al., 2019) and the first stage of tectonic uplift (93–80 Ma; Fig. 11). Yet it appears to be a time lag between our mineralogical and geochemical data and the evolution of sedimentation rates in the Cape basin, as the maximum of I + C/S and $\Delta\varepsilon_{Hf}$ occurs by the Danian while the period of high sedimentation rates extents only until the Maastrichtian-Danian boundary. Again, this time lag is likely not linked to uncertainties in site 361 age model, as the Maastrichtian-Danian boundary is well identified. The origin of his time lag remains unclear. Additional data from more proximal sites may bring further insights into this question in the future.

Although additional studies are needed to better constrain the regional controls of the uplift and to sediment routing, we favor the late stage of the tectonic uplift (80–70 Ma) in the southwestern part of the South African Plateau as the main forcing mechanisms in the enhancement in denudation processes recorded in the Cape Basin during the Campanian-Danian interval.

Relief formation on the southwestern African margin may explain the contrasting regional climate change offshore and onshore that seems to appear from palynological studies during the late Cretaceous (Braun et al., 2014). This data suggested an evolution from arid to humid conditions offshore, and from humid to arid conditions onshore, further supported by the increase in palygorskite proportions identified in our dataset. If confirmed by additional data, this apparent divergence between offshore and onshore climate data may be reconciled by relief

formation during the late stage uplift of the South African plateau, that may have led to inland aridification while favouring condensation of clouds on the escarpment facing the ocean thus causing more humid conditions (i.e., Rain-Shadow effect; Roe, 2005; Siler et al., 2013). This hypothesis still requires further palynological data; which remains rather localized from sites relatively far apart, and further clay mineralogical studies to better constrain the extent of the area affected by these changes in hydrolysing conditions.

The global climatic cooling trend evidenced by benthic (Fig. 8; Friedrich et al., 2012; O'Brien et al., 2017) and planktonic foraminifera $\delta^{18}O$ and Tex_{86} records initiated after the Turonian, earlier than the recorded increase in continental chemical weathering suggested by our data which occurs during the Campanian-Danian interval. Hence, it is unlikely that changes in weathering processes linked to the South African Plateau uplift triggered this shift toward cooler conditions. Yet they could have contributed to maintain overall cooler climatic conditions after the Campanian. The potential role of this process in the late Cretaceous climate evolution has already been pointed out by $\Delta\varepsilon_{Hf}$ records on the eastern south American margin (Corentin et al., 2022, 2023). Our new data set further supports this hypothesis and suggests that tectonically induced enhanced silicate chemical weathering could have occurred over a large region of the globe extending to Southern Africa.

6. Conclusions

Our study presents the evolution of physical erosion and silicate chemical weathering on the South African plateau during the late Cretaceous (100–66 Ma), using clay mineral assemblages and Hf—Nd isotopic compositions of clay fractions from the DSDP core 361 located at the Cape Basin.

TEM imagery and REE analyses indicate that the clay minerals are predominantly detrital and thus reflect the changes in denudation. Overall, the clay mineral assemblages and $\Delta\varepsilon_{Hf}$ show a concomitant enhancement of both physical erosion and silicate chemical weathering during the Campanian-Danian interval (ca. 77–62 Ma). This increase occurred likely in response to the late stage of the tectonic uplift of the South African plateau during the Campanian-Maastrichtian interval (ca. 80–70 Ma), although the lag between the record and the uplift timing still requires further investigation. Regardless, It seems that in this context tectonics played a major role compared to climate, in fact the tectonic forcing seems to have had an impact on the regional climate through the evolution of a rain-shadow effect, while the impact in the global climate cooling through the drawdown of atmospheric CO_2 product of the enhancement in silicate weathering reactions seems to be minor, as the main cooling phase had occurred already in the Turonian (ca. 93 Ma).

Declaration of Competing Interest

The authors declare the following financial interests/personal relationships which may be considered as potential competing interests:

We report that financial support was provided by European Union's Horizon 2020 research and innovation program under the Marie Sklodowska-Curie grant agreement No 860383.

Data availability

All the data are provided in the supplementary materials attached to this paper.

Acknowledgments

We thank IODP for providing access to the material. This project has received funding from the European Union's Horizon 2020 research and innovation program under the Marie Sklodowska-Curie grant agreement No 860383 and from the ANR RISE. We thank Rémi Chassagnon (Laboratory ICB and analytical platform ARCEN, University of Burgundy) for TEM observations realized at INRAe of Dijon, Ludovic Bruneau of the Biogéosciences Laboratory and GISMO analytical Platform (University of Burgundy) for the XRD analyses, Marie-Laure Rouget and Bleuenn Gueguen of the Pôle Spectrométrie Océan (Brest), Olivier Reubi of the Institut des Sciences de la Terre (ISTE-Lausanne), and Philippe Telouk of the ENS Lyon for their analytical support. We thank the reviewers for their constructive comments improving the discussion and the manuscript in general. Special thanks to Christopher P.A Smith for his comments and suggestions during the redaction of the manuscript.

Appendix A. Supplementary data

Supplementary data to this article can be found online at https://doi.org/10.1016/j.margeo.2023.107187.

References

Adams, B.A., Whipple, K.X., Forte, A.M., Heimsath, A.M., Hodges, K.V., 2020. Climate controls on erosion in tectonically active landscapes. Sci. Adv. 6, eaaz3166. https://doi.org/10.1126/sciadv.aaz3166.

Adatte, T., Bolle, M.-P., Kaenel, E.D., Gawenda, P., Winkler, W., Von Salis, K., 2000. Climatic evolution from Paleocene to earliest Eocene inferred from clay-minerals: a transect from northern Spain (Zumaya) to southern (Spain, Tunisia) and southeastern Tethys margins (Israel, Negev). GFF 122, 7–8. https://doi.org/10.1080/11035890001221007.

Allen, P.A., Densmore, A.L., 2000. Sediment flux from an uplifting fault block. Basin Res. 12, 367–380. https://doi.org/10.1111/j.1365-2117.2000.00135.x.

Armitage, J.J., Dunkley Jones, T., Duller, R.A., Whittaker, A.C., Allen, P.A., 2013. Temporal buffering of climate-driven sediment flux cycles by transient catchment response. Earth Planet. Sci. Lett. 369–370, 200–210. https://doi.org/10.1016/j.epsl.2013.03.020.

Baby, G., Guillocheau, F., Braun, J., Robin, C., Dall'Asta, M., 2019. Solid sedimentation rates history of the Southern African continental margins: Implications for the uplift history of the South African Plateau. Terra Nova 32, 53–65. https://doi.org/10.1111/ter.12435.

Bamford, M.K., de Wit, M.C., 1993. Taxonomic description of fossil wood from Cainozoic Sak river terraces, near Brandvlei, Bushmanland, South Africa. Palaeontol. Afr. 30, 71–80.

Bamford, M.K., Stevenson, I.R., 2002. A submerged late Cretaceous podocarpaceous forest, west coast, South Africa. South Afr. J. Sci. 98, 181–185.

Barrat, J.A., Keller, F., Amossé, J., Taylor, R.N., Nesbitt, R.W., Hirata, T., 1996. Determination of rare earth elements in sixteen silicate reference samples by ICP-MS after tm addition and ion exchange separation. Geostand. Geoanal. Res. 20, 133–139. https://doi.org/10.1111/j.1751-908X.1996.tb00177.x.

Bayon, G., German, C.R., Boella, R.M., Milton, J.A., Taylor, R.N., Nesbitt, R.W., 2002. An improved method for extracting marine sediment fractions and its application to Sr and Nd isotopic analysis. Chem. Geol. 187, 179–199. https://doi.org/10.1016/S0009-2541(01)00416-8.

Bayon, G., Vigier, N., Burton, K.W., Jean Carignan, A.B., Etoubleau, J., Chu, N.-C., 2006. The control of weathering processes on riverine and seawater hafnium isotope ratios. Geology 34, 433. https://doi.org/10.1130/G22130.1.

Bayon, G., Barrat, J., Etoubleau, J., Benoit, M., Bollinger, C., Révillon, S., 2009. Determination of Rare Earth Elements, Sc, Y, Zr, Ba, Hf and Th in Geological Samples by ICP-MS after Tm Addition and Alkaline Fusion 12.

Bayon, G., Dennielou, B., Etoubleau, J., Ponzevera, E., Toucanne, S., Bermell, S., 2012. Intensifying Weathering and Land Use in Iron Age Central Africa. Science 335, 1219–1222. https://doi.org/10.1126/science.1215400.

Bayon, G., Toucanne, S., Skonieczny, C., André, L., Bermell, S., Cheron, S., Dennielou, B., Etoubleau, J., Freslon, N., Gauchery, T., Germain, Y., Jorry, S.J., Ménot, G., Monin, L., Ponzevera, E., Rouget, M.-L., Tachikawa, K., Barrat, J.A., 2015. Rare earth elements and neodymium isotopes in world river sediments revisited. Geochim. Cosmochim. Acta 170, 17–38. https://doi.org/10.1016/j.gca.2015.08.001.

Bayon, G., Skonieczny, C., Delvigne, C., Toucanne, S., Bermell, S., Ponzevera, E., André, L., 2016. Environmental Hf–Nd isotopic decoupling in World river clays. Earth Planet. Sci. Lett. 438, 25–36. https://doi.org/10.1016/j.epsl.2016.01.010.

Bolli, H.M., Ryan, W.B.F., Foresman, J.B., Hottman, W.E., Kagami, H., Longoria, J.F., McKnight, B.K., Melguen, M., Natland, J., Proto-Decima, F., Siesser, W.G., 1978. Cape Basin Continental Rise Sites 360 and 361 (No. 40), Initial Reports of the Deep Sea Drilling Project, 40. Deep Sea Drilling Project. https://doi.org/10.2973/dsdp.proc.40.1978.

Bougeault, C., Pellenard, P., Deconinck, J.-F., Hesselbo, S.P., Dommergues, J.-L., Bruneau, L., Cocquerez, T., Laffont, R., Huret, E., Thibault, N., 2017. Climatic and palaeoceanographic changes during the Pliensbachian (early Jurassic) inferred from clay mineralogy and stable isotope (C-O) geochemistry (NW Europe). Glob. Planet. Chang. 149, 139–152. https://doi.org/10.1016/j.gloplacha.2017.01.005.

Bouvier, A., Vervoort, J.D., Patchett, P.J., 2008. The Lu–Hf and Sm–Nd isotopic composition of CHUR: constraints from unequilibrated chondrites and implications

for the bulk composition of terrestrial planets. Earth and Planet. Sci. Lett. 273 (1–2), 48–57.
Braun, J., Guillocheau, F., Robin, C., Baby, G., Jelsma, H., 2014. Rapid erosion of the Southern African Plateau as it climbs over a mantle superswell: Eroding southern African Plateau. J. Geophys. Res. Solid Earth 119, 6093–6112. https://doi.org/10.1002/2014JB010998.
Brown, R., Summerfield, M., Gleadow, A., Gallagher, K., Carter, A., Beucher, R., Wildman, M., 2014. Intracontinental deformation in southern Africa during the Late Cretaceous. J. African Earth Sci. 100, 20–41.
Burbank, D.W., Anderson, R.S., 2012. Tectonic Geomorphology, 2. ed. Wiley-Blackwell, Chichester Oxford.
Carpentier, M., Weis, D., Chauvel, C., 2014. Fractionation of Sr and Hf isotopes by mineral sorting in Cascadia Basin terrigenous sediments. Chem. Geol. 382, 67–82. https://doi.org/10.1016/j.chemgeo.2014.05.028.
Castelltort, S., Van Den Driessche, J., 2003. How plausible are high-frequency sediment supply-driven cycles in the stratigraphic record? Sediment. Geol. 157, 3–13. https://doi.org/10.1016/S0037-0738(03)00066-6.
Catuneanu, O., Wopfner, H., Eriksson, P.G., Cairncross, B., Rubidge, B.S., Smith, R.M.H., Hancox, P.J., 2005. The Karoo basins of south-Central Africa. J. Afr. Earth Sci. 43, 211–253. https://doi.org/10.1016/j.jafrearsci.2005.07.007.
Chamley, H., 1989. Clay Sedimentology. Springer Science & Business Media.
Chamley, H., 1981. Long-Term Trends in Clay Deposition in the Ocean. Oceanol. Acta Spec. Issue.
Chauvel, C., Garçon, M., Bureau, S., Besnault, A., Jahn, B., Ding, Z., 2014. Constraints from loess on the Hf–Nd isotopic composition of the upper continental crust. Earth Planet. Sci. Lett. 388, 48–58. https://doi.org/10.1016/j.epsl.2013.11.045.
Chemale, F., Scheepers, R., Gresse, P.G., Van Schmus, W.R., 2011. Geochronology and sources of late Neoproterozoic to Cambrian granites of the Saldania Belt. Int. J. Earth Sci. 100, 431–444. https://doi.org/10.1007/s00531-010-0579-1.
Chenot, E., Deconinck, J.-F., Pucéat, E., Pellenard, P., Guiraud, M., Jaubert, M., Jarvis, I., Thibault, N., Cocquerez, T., Bruneau, L., Razmjooei, M.J., Boussaha, M., Richard, J., Sizun, J.-P., Stemmerik, L., 2018. Continental weathering as a driver of late Cretaceous cooling: new insights from clay mineralogy of Campanian sediments from the southern Tethyan margin to the Boreal realm. Glob. Planet. Chang. 162, 292–312. https://doi.org/10.1016/j.gloplacha.2018.01.016.
Chu, N.-C., Taylor, R.N., Chavagnac, V., Nesbitt, R.W., Boella, R.M., Milton, J.A., German, C.R., Bayon, G., Burton, K., 2002. Hf isotope ratio analysis using multi-collector inductively coupled plasma mass spectrometry: an evaluation of isobaric interference corrections. J. Anal. At. Spectrom. 17, 1567–1574. https://doi.org/10.1039/b206707b.
Clauer, N., 1990. Morphological, Chemical, and Isotopic evidence for an early Diagenetic Evolution of Detrital Smectite in Marine Sediments. Clay Clay Miner. 38, 33–46. https://doi.org/10.1346/CCMN.1990.0380105.
Corentin, P., Pucéat, E., Pellenard, P., Freslon, N., Guiraud, M., Blondet, J., Adatte, T., Bayon, G., 2022. Hafnium-neodymium isotope evidence for enhanced weathering and uplift-climate interactions during the late Cretaceous. Chem. Geol. 591, 120724 https://doi.org/10.1016/j.chemgeo.2022.120724.
Corentin, P., Pucéat, E., Pellenard, P., Guiraud, M., Blondet, J., Bayon, G., Adatte, T., 2023. Late Cretaceous evolution of chemical weathering at the northeastern south American margin inferred from mineralogy and Hf-Nd isotopes. Mar. Geol. 455, 106968 https://doi.org/10.1016/j.margeo.2022.106968.
Davey, R.J., 1978. 25. MARINE CRETACEOUS PALYNOLOGY OF SITE 361. In: DSDP LEG, 40. OFF SOUTHWESTERN AFRICA.
De Wit, 1999. Post-Gondwana drainage and the development of diamond placers in western South Africa. Econ. Geol. 94 (5), 721–740.
De Wit, M.C.J., Ward, J.D., Bamford, M.K., Roberts, M.J., 2009. The significance of the cretaceous diamondiferous gravel deposit at Mahura Muthla, northern cape province, South Africa. South Afr. J. Geol. 112, 89–108. https://doi.org/10.2113/gssajg.112.2.89.
Dera, G., Pellenard, P., Neige, P., Deconinck, J.-F., Pucéat, E., Dommergues, J.-L., 2009. Distribution of clay minerals in early Jurassic Peritethyan seas: Palaeoclimatic significance inferred from multiproxy comparisons. Palaeogeogr. Palaeoclimatol. Palaeoecol. 271, 39–51. https://doi.org/10.1016/j.palaeo.2008.09.010.
Dia, A., Allègre, C.J., Erlank, A.J., 1990. The development of continental crust through geological time: the south African case. Earth Planet. Sci. Lett. 98, 74–89. https://doi.org/10.1016/0012-821X(90)90089-G.
Dollar, E.S.J., 1998. Palaeofluvial geomorphology in southern Africa: a review. Prog. Phys. Geogr. 22, 325–349. https://doi.org/10.1177/030913339802200302.
Dummann, W., Steinig, S., Hofmann, P., Flögel, S., Osborne, A.H., Frank, M., Herrle, J.O., Bretschneider, L., Sheward, R.M., Wagner, T., 2020. The impact of early Cretaceous gateway evolution on ocean circulation and organic carbon burial in the emerging South Atlantic and Southern Ocean basins. Earth Planet. Sci. Lett. 530, 115890 https://doi.org/10.1016/j.epsl.2019.115890.
Eglington, B.M., Armstrong, R.A., 2004. The Kaapvaal Craton and adjacent orogens, southern Africa: a geochronological database and overview of the geological development of the craton. South Afr. J. Geol. 107, 13–32. https://doi.org/10.2113/107.1-2.13.
Fagel, N., André, L., Chamley, H., Debrabant, P., Jolivet, L., 1992. Clay sedimentation in the Japan Sea since the early Miocene: influence of source-rock and hydrothermal activity. Sediment. Geol. 80, 27–40. https://doi.org/10.1016/0037-0738(92)90029-Q.
Fagel, N., Robert, C., Preda, M., Thorez, J., 2001. Smectite composition as a tracer of deep circulation: the case of the Northern North Atlantic. Mar. Geol. 172, 309–330. https://doi.org/10.1016/S0025-3227(00)00123-7.
Flowers, R.M., Schoene, B., 2010. (U-Th)/he thermochronometry constraints on unroofing of the eastern Kaapvaal craton and significance for uplift of the southern African Plateau. Geology 38, 827–830. https://doi.org/10.1130/G30980.1.
Frank, M., 2002. Radiogenic Isotopes: Tracers of Past Ocean Circulation and Erosional Input. Rev. Geophys. 40 https://doi.org/10.1029/2000RG000094, 1-1-1–38.
Frank, T.D., Arthur, M.A., 1999. Tectonic forcings of Maastrichtian Ocean-climate evolution. Paleoceanography 14, 103–117. https://doi.org/10.1029/1998PA900017.
Freslon, N., Bayon, G., Birot, D., Bollinger, C., Barrat, J.A., 2011. Determination of rare earth elements and other trace elements (Y, Mn, Co, Cr) in seawater using Tm addition and Mg(OH)2 co-precipitation. Talanta 85, 582–587. https://doi.org/10.1016/j.talanta.2011.04.023.
Friedrich, O., Norris, R.D., Erbacher, J., 2012. Evolution of middle to late Cretaceous oceans—a 55 m.y. record of Earth's temperature and carbon cycle. Geology 40, 107–110. https://doi.org/10.1130/G32701.1.
Gabet, E., Mudd, S., 2009. A theoretical model coupling chemical weathering rate with denudation rates. Geology 37, 151–154. https://doi.org/10.1130/G25270A.1.
Garçon, M., Boyet, M., Carlson, R.W., Horan, M.F., Auclair, D., Mock, T.D., 2018. Factors influencing the precision and accuracy of Nd isotope measurements by thermal ionization mass spectrometry. Chem. Geol. 476, 493–514.
Garçon, M., Chauvel, C., France-Lanord, C., Huyghe, P., Lavé, J., 2013. Continental sedimentary processes decouple Nd and Hf isotopes. Geochim. Cosmochim. Acta 121, 177–195. https://doi.org/10.1016/j.gca.2013.07.027.
Garçon, M., Chauvel, C., France-Lanord, C., Limonta, M., Garzanti, E., 2014. Which minerals control the Nd–Hf–Sr–Pb isotopic compositions of river sediments? Chem. Geol. 364, 42–55. https://doi.org/10.1016/j.chemgeo.2013.11.018.
Garzanti, E., Padoan, M., Setti, M., López-Galindo, A., Villa, I.M., 2014. Provenance versus weathering control on the composition of tropical river mud (southern Africa). Chem. Geol. 366, 61–74. https://doi.org/10.1016/j.chemgeo.2013.12.016.
Garzanti, E., Pastore, G., Stone, A., Vainer, S., Vermeesch, P., Resentini, A., 2022. Provenance of Kalahari Sand: Paleoweathering and recycling in a linked fluvial-aeolian system. Earth Sci. Rev. 224, 103867 https://doi.org/10.1016/j.earscirev.2021.103867.
Goldstein, S.L., Hemming, S.R., 2003. Long-lived isotopic tracers in oceanography, paleoceanography, and ice-sheet dynamics. Treat. Geochem. 6, 625.
Goudie, A.S., 2005. The drainage of Africa since the Cretaceous. Geomorphology 67, 437–456. https://doi.org/10.1016/j.geomorph.2004.11.008.
Gradstein, F., Ogg, J., Schmitz, M., Ogg, G., 2012. The Geologic Time Scale 2012, vol. 1. Elsevier, Amsterdam Heidelberg.
Green, P.F., Duddy, I.R., Japsen, P., Bonow, J.M., Malan, J.A., 2017. Post-breakup burial and exhumation of the southern margin of Africa. Basin Res. 29, 96–127. https://doi.org/10.1111/bre.12167.
Guillocheau, F., Rouby, D., Robin, C., Helm, C., Rolland, N., De Veslud, Braun, J., 2012. Quantification and causes of the terrigeneous sediment budget at the scale of a continental margin: a new method applied to the Namibia–South Africa margin. Basin Res. 24 (1), 3–30.
Gutjahr, M., Frank, M., Stirling, C.H., Klemm, V., van de Flierdt, T., Halliday, A.N., 2007. Reliable extraction of a Deepwater trace metal isotope signal from Fe–Mn oxyhydroxide coatings of marine sediments. Chem. Geol. 242, 351–370. https://doi.org/10.1016/j.chemgeo.2007.03.021.
Haddon, I.G., McCarthy, T.S., 2005. The Mesozoic–Cenozoic interior sag basins of Central Africa: The Late-Cretaceous–Cenozoic Kalahari and Okavango basins. J. Afr. Earth Sci. 43, 316–333. https://doi.org/10.1016/j.jafrearsci.2005.07.008.
Harnois, L., 1988. The CIW index: a new chemical index of weathering. Sediment. Geol. 55, 319–322. https://doi.org/10.1016/0037-0738(88)90137-6.
Hawkesworth, C.J., Marsh, J.S., Duncan, A.R., Erlank, A.J., Norry, M.J., 1984. The Role of Continental Lithosphere in the Generation of the Karoo Volcanic Rocks: Evidence from Combined Nd-and Sr-Isotope Studies.
Herman, F., Seward, D., Valla, P.G., Carter, A., Kohn, B., Willett, S.D., Ehlers, T.A., 2013. Worldwide acceleration of mountain erosion under a cooling climate. Nature 504, 423–426. https://doi.org/10.1038/nature12877.
Huber, B.T., MacLeod, K.G., Watkins, D.K., Coffin, M.F., 2018. The rise and fall of the Cretaceous Hot Greenhouse climate. Glob. Planet. Chang. 167, 1–23. https://doi.org/10.1016/j.gloplacha.2018.04.004.
Jeandel, C., Arsouze, T., Lacan, F., Téchiné, P., Dutay, J.-C., 2007. Isotopic Nd compositions and concentrations of the lithogenic inputs into the ocean: a compilation, with an emphasis on the margins. Chem. Geol. 239, 156–164. https://doi.org/10.1016/j.chemgeo.2006.11.013.
Jochum, K.P., Weis, U., Schwager, B., Stoll, B., Wilson, S.A., Haug, G.H., Andreae, M.O., Enzweiler, J., 2016. Reference values following ISO guidelines for frequently requested rock reference materials. Geostand. Geoanal. Res. 40, 333–350. https://doi.org/10.1111/j.1751-908X.2015.00392.x.
John, C.M., Banerjee, N.R., Longstaffe, F.J., Sica, C., Law, K.R., Zachos, J.C., 2012. Clay assemblage and oxygen isotopic constraints on the weathering response to the Paleocene-Eocene thermal maximum, east coast of North America. Geology 40, 591–594. https://doi.org/10.1130/G32785.1.
Kemp, S.J., Ellis, M.A., Mounteney, I., Kender, S., 2016. Palaeoclimatic implications of high-resolution clay mineral assemblages preceding and across the onset of the Palaeocene–Eocene Thermal Maximum, North Sea Basin. Clay Miner. 51, 793–813. https://doi.org/10.1180/claymin.2016.051.5.08.
Knidiri, A., Daoudi, L., Ouahabi, M.E., Rhouta, B., Rocha, F., Fagel, N., 2014. Palaeogeographic controls on palygorskite occurrence in Maastrichtian-Palaeogene sediments of the Western High Atlas and Meseta Basins (Morocco). Clay Miner. 49, 595–608. https://doi.org/10.1180/claymin.2014.049.4.08.
Kounov, A., Viola, G., de Wit, M., Andreoli, M.A.G., 2009. Denudation along the Atlantic passive margin: new insights from apatite fission-track analysis on the western coast

of South Africa. Geol. Soc. Lond. Spec. Publ. 324, 287–306. https://doi.org/10.1144/SP324.19.
Kounov, A., Viola, G., Dunkl, I., Frimmel, H.E., 2013. Southern African perspectives on the long-term morpho-tectonic evolution of cratonic interiors. Tectonophysics 601, 177–191. https://doi.org/10.1016/j.tecto.2013.05.009.
Lanson, B., Sakharov, B., Claret, F., Drits, V., 2009. Diagenetic smectite-to-illite transition in clay-rich sediments: a reappraisal of X-ray diffraction results using the multi-specimen method. Am. J. Sci. 309, 476–516. https://doi.org/10.2475/06.2009.03.
Laveuf, C., Cornu, S., Guilherme, L.R.G., Guerin, A., Juillot, F., 2012. The impact of redox conditions on the rare earth element signature of redoximorphic features in a soil sequence developed from limestone. Geoderma 170, 25–38. https://doi.org/10.1016/j.geoderma.2011.10.014.
Louvat, P., Allègre, C.J., 1997. Present denudation rates on the island of Réunion determined by river geochemistry: Basalt weathering and mass budget between chemical and mechanical erosions. Geochim. Cosmochim. Acta 61, 3645–3669. https://doi.org/10.1016/S0016-7037(97)00180-4.
Millot, R., Gaillardet, J., Dupré, B., Allègre, C.J., 2002. The global control of silicate weathering rates and the coupling with physical erosion: new insights from rivers of the Canadian Shield. Earth Planet. Sci. Lett. 196, 83–98. https://doi.org/10.1016/S0012-821X(01)00599-4.
Moore, D.M., Reynolds, J.R.J., 1989. X-Ray Diffraction and the Identification and Analysis of Clay Minerals, Second edition. ed. Oxford University Press, London.
Münker, C., Weyer, S., Scherer, E., Mezger, K., 2001. Separation of high field strength elements (Nb, Ta, Zr, Hf) and Lu from rock samples for MC-ICPMS measurements. Geochem. Geophys. Geosyst. 2 (12).
Murphy, D.P., Thomas, D.J., 2013. The evolution of late Cretaceous deep-ocean circulation in the Atlantic basins: neodymium isotope evidence from South Atlantic drill sites for tectonic controls. Geochem. Geophys. Geosyst. 14, 5323–5340. https://doi.org/10.1002/2013GC004889.
Nadeau, P.H., Wilson, M.J., McHardy, W.J., Tait, J.M., 1985. The conversion of smectite to illite during diagenesis: evidence from some illitic clays from bentonites and sandstones. Mineral. Mag. 49, 393–400. https://doi.org/10.1180/minmag.1985.049.352.10.
NASA, J.P.L., 2013. NASA Shuttle Radar Topography Mission Global 30 Arc Second. https://doi.org/10.5067/MEASURES/SRTM/SRTMGL30.002.
Natland, J.H., 1978. Composition, Provenance, and Diagenesis of Cretaceous Clastic Sediments Drilled on the Atlantic Continental Rise off Southern Africa, DSDP Site 361. Implications for the Early Circulation of the South Atlantic.
Nesbitt, H.W., Young, G.M., 1982. Early Proterozoic climates and plate motions inferred from major element chemistry of lutites. Nature 299, 715–717. https://doi.org/10.1038/299715a0.
O'Brien, C.L., Robinson, S.A., Pancost, R.D., Sinninghe Damsté, J.S., Schouten, S., Lunt, D.J., Alsenz, H., Bornemann, A., Bottini, C., Brassell, S.C., Farnsworth, A., Forster, A., Huber, B.T., Inglis, G.N., Jenkyns, H.C., Linnert, C., Littler, K., Markwick, P., McAnena, A., Mutterlose, J., Naafs, B.D.A., Püttmann, W., Sluijs, A., van Helmond, N.A.G.M., Vellekoop, J., Wagner, T., Wrobel, N.E., 2017. Cretaceous sea-surface temperature evolution: Constraints from TEX86 and planktonic foraminiferal oxygen isotopes. Earth Sci. Rev. 172, 224–247. https://doi.org/10.1016/j.earscirev.2017.07.012.
Parker, A., 1970. An Index of Weathering for Silicate Rocks. Geol. Mag. 107, 501–504. https://doi.org/10.1017/S0016756800058581.
Patchett, P.J., White, W.M., Feldmann, H., Kielinczuk, S., Hofmann, A.W., 1984. Hafnium/rare earth element fractionation in the sedimentary system and crustal recycling into the Earth's mantle. Earth Planet. Sci. Lett. 69, 365–378. https://doi.org/10.1016/0012-821X(84)90195-X.
Petschick, R., 2001. MacDiff Ver. 4.2.5.
Pin, C., Zalduegui, J.S., 1997. Sequential separation of light rare-earth elements, thorium and uranium by miniaturized extraction chromatography: application to isotopic analyses of silicate rocks. Analytica Chimica Acta 339 (1–2), 79–89.
Pletsch, T., 2001. Palaeoenvironmental implications of palygorskite clays in Eocene deep-water sediments from the western Central Atlantic. Geol. Soc. Lond. Spec. Publ. 183, 307–316. https://doi.org/10.1144/GSL.SP.2001.183.01.15.
Pletsch, T., Daoudi, L., Chamley, H., Deconinck, J.F., Charroud, M., 1996. Palaeogeographic controls on palygorskite occurrence in mid-Cretaceous sediments of Morocco and adjacent basins. Clay Miner. 31, 403–416. https://doi.org/10.1180/claymin.1996.031.3.10.
Price, J.R., Velbel, M.A., Patino, L.C., 2005. Rates and time scales of clay-mineral formation by weathering in saprolitic regoliths of the southern Appalachians from geochemical mass balance. Geol. Soc. Am. Bull. 117, 783. https://doi.org/10.1130/B25547.1.
Raab, M.J., Brown, R.W., Gallagher, K., Carter, A., Weber, K., 2002. Late Cretaceous reactivation of major crustal shear zones in northern Namibia: constraints from apatite fission track analysis. Tectonophysics 349, 75–92. https://doi.org/10.1016/S0040-1951(02)00047-1.
Rayner, R.J., Bamford, M.K., Brothers, D.J., Dippenaar-Schoeman, A.S., McKay, I.J., Oberprieler, R.G., Watersl, S.B., 1997. Cretaceous Fossils from the Orapa Diamond Mine 11.
Reid, D.L., 1997. Sm-Nd age and REE geochemistry of Proterozoic arc-related igneous rocks in the Richtersveld subprovince, Namaqua Mobile Belt, Southern Africa. J. Afr. Earth Sci. 24, 621–633. https://doi.org/10.1016/S0899-5362(97)00084-5.
Robert, C., 1987. Clay Mineral Associations and Structural Evolution of the South. Jurassic to Eocene, Atlantic.
Roe, G.H., 2005. Orographic precipitation. Annu. Rev. Earth Planet. Sci. 33, 645–671. https://doi.org/10.1146/annurev.earth.33.092203.122541.
Romans, B.W., Castelltort, S., Covault, J.A., Fildani, A., Walsh, J.P., 2016. Environmental signal propagation in sedimentary systems across timescales. Earth Sci. Rev. 153, 7–29. https://doi.org/10.1016/j.earscirev.2015.07.012.
Rouby, D., Bonnet, S., Guillocheau, F., Gallagher, K., Robin, C., Biancotto, F., Dauteuil, O., Braun, J., 2009. Sediment supply to the Orange sedimentary system over the last 150My: an evaluation from sedimentation/denudation balance. Mar. Pet. Geol. 26, 782–794. https://doi.org/10.1016/j.marpetgeo.2008.08.004.
Ruffell, A., McKinley, J.M., Worden, R.H., 2002. Comparison of clay mineral stratigraphy to other proxy palaeoclimate indicators in the Mesozoic of NW Europe. Philos. Trans. R. Soc. Lond. Ser. Math. Phys. Eng. Sci. 360, 675–693. https://doi.org/10.1098/rsta.2001.0961.
Sandersen, A., 2006. A Palynological Investigation of the Offshore Cretaceous Sequence on the South-West Coast of South Africa.
Schlüter, T., 2008. Geological Atlas of Africa. Springer.
Schoene, B., Dudas, F.O.L., Bowring, S.A., De Wit, M., 2009. Sm–Nd isotopic mapping of lithospheric growth and stabilization in the eastern Kaapvaal craton. Terra Nova 21, 219–228. https://doi.org/10.1111/j.1365-3121.2009.00877.x.
Setti, M., Marinoni, L., López-Galindo, A., 2004. Mineralogical and geochemical characteristics (major, minor, trace elements and *REE*) of detrital and authigenic clay minerals in a Cenozoic sequence from Ross Sea, Antarctica. Clay Miner. 39, 405–421. https://doi.org/10.1180/000985503540143.
Siler, N., Roe, G., Durran, D., 2013. On the dynamical causes of variability in the rain-shadow effect: a case study of the washington cascades. J. Hydrometeorol. 14, 122–139. https://doi.org/10.1175/JHM-D-12-045.1.
Smirnova, E.V., Flem, B., Anchutina, E.A., Mysovskaya, I.N., Lozhkin, V.I., Petrov, L.L., 2010. Determination of REE, Y, Nb, Zr, Hf, Ta, Th and U in geological reference materials LSHC-1 and Amf-1 by solution and laser ablation ICP-MS. Geostand. Geoanal. Res. 34, 49–65. https://doi.org/10.1111/j.1751-908X.2009.00009.x.
Smith, R.M.H., 1986. Sedimentation and palaeoenvironments of late Cretaceous crater-lake deposits in Bushmanland, South Africa. Sedimentology 33, 369–386. https://doi.org/10.1111/j.1365-3091.1986.tb00542.x.
Smith, R.M.H., 1988. Palaeoenvironmental reconstruction of a Cretaceous crater-lake deposit in Bushmanland, South Africa. Collect. Palaeoecol. Afr. Surround. Isl. 27–41.
Stanley, J.R., Flowers, R.M., 2020. Mesozoic denudation history of the lower Orange River and eastward migration of erosion across the southern African Plateau. Lithosphere 12, 74–87. https://doi.org/10.1130/L1121.1.
Stanley, J.R., Flowers, R.M., Bell, D.R., 2013. Kimberlite (U-Th)/he dating links surface erosion with lithospheric heating, thinning, and metasomatism in the southern African Plateau. Geology 41, 1243–1246. https://doi.org/10.1130/G34797.1.
Stanley, J.R., Braun, J., Baby, G., Guillocheau, F., Robin, C., Flowers, R.M., Brown, R., Wildman, M., Beucher, R., 2021. Constraining plateau uplift in Southern Africa by combining thermochronology, sediment flux, topography, and landscape evolution modeling. J. Geophys. Res. Solid Earth 126. https://doi.org/10.1029/2020JB021243.
Svensen, H., Corfu, F., Polteau, S., Hammer, Ø., Planke, S., 2012. Rapid magma emplacement in the Karoo large igneous province. Earth Planet. Sci. Lett. 325, 1–9.
Tanaka, T., Togashi, S., Kamioka, H., Amakawa, H., Kagami, H., Hamamoto, T., Yuhara, M., Orihashi, Y., Yoneda, S., Shimizu, H., Kunimaru, T., Takahashi, K., Yanagi, T., Nakano, T., Fujimaki, H., Shinjo, R., Asahara, Y., Tanimizu, M., Dragusanu, C., 2000. JNdi-1: a neodymium isotopic reference in consistency with LaJolla neodymium. Chem. Geol. 168, 279–281. https://doi.org/10.1016/S0009-2541(00)00198-4.
Tankard, A.J., Martin, M., Eriksson, K.A., Hobday, D.K., Hunter, D.R., Minter, W.E.L., 1982. Crustal Evolution of Southern Africa: 3.8 Billion Years of Earth History. Springer Science & Business Media.
Taylor, S.R., McLennan, S.M., 1985. The Continental Crust: Its Composition and Evolution.
Thiry, M., 2000. Palaeoclimatic interpretation of clay minerals in marine deposits: an outlook from the continental origin. Earth Sci. Rev. 49, 201–221. https://doi.org/10.1016/S0012-8252(99)00054-9.
Thiry, M., Pletsch, T., 2011. Palygorskite clays in marine sediments: records of extreme climate. In: *Developments in Clay Science*, 3. Elsevier, pp. 101–124.
Tinker, J., de Wit, M., Brown, R., 2008. Mesozoic exhumation of the southern Cape, South Africa, quantified using apatite fission track thermochronology. Tectonophysics 455, 77–93. https://doi.org/10.1016/j.tecto.2007.10.009.
Tofelde, S., Bernhardt, A., Guerit, L., Romans, B.W., 2021. Times associated with source-to-sink propagation of environmental signals during landscape transience. Front. Earth Sci. 9, 628315 https://doi.org/10.3389/feart.2021.628315.
Vainer, S., Erel, Y., Matmon, A., 2018. Provenance and depositional environments of quaternary sediments in the southern Kalahari Basin. Chem. Geol. 476, 352–369. https://doi.org/10.1016/j.chemgeo.2017.11.031.
Vervoort, J.D., Blichert-Toft, J., 1999. Evolution of the depleted mantle: Hf isotope evidence from juvenile rocks through time. Geochim. Cosmochim. Acta 63, 533–556. https://doi.org/10.1016/S0016-7037(98)00274-9.
Vervoort, J.D., Plank, T., Prytulak, J., 2011. The Hf–Nd isotopic composition of marine sediments. Geochim. Cosmochim. Acta 75, 5903–5926. https://doi.org/10.1016/j.gca.2011.07.046.
Weis, D., Kieffer, B., Maerschalk, C., Pretorius, W., Barling, J., 2005. High-precision Pb-Sr-Nd-Hf isotopic characterization of USGS BHVO-1 and BHVO-2 reference materials: Pb-Sr-Nd-Hf CHARACTERIZATION. Geochem. Geophys. Geosyst. 6 https://doi.org/10.1029/2004GC000852.
Whipple, K.X., 2014. Can erosion drive tectonics? Science 346, 918–919. https://doi.org/10.1126/science.aaa0887.
Whipple, K.X., Meade, B., 2006. Orogen response to changes in climatic and tectonic forcing. Earth Planet. Sci. Lett. 11.

Wildman, M., Brown, R., Watkins, R., Carter, A., Gleadow, A., Summerfield, M., 2015. Post break-up tectonic inversion across the southwestern cape of South Africa: new insights from apatite and zircon fission track thermochronometry. Tectonophysics 654, 30–55. https://doi.org/10.1016/j.tecto.2015.04.012.

Wildman, M., Brown, R., Beucher, R., Persano, C., Stuart, F., Gallagher, K., Schwanethal, J., Carter, A., 2016. The chronology and tectonic style of landscape evolution along the elevated Atlantic continental margin of South Africa resolved by joint apatite fission track and (U-Th-Sm)/He thermochronology. Tectonics 35, 511–545. https://doi.org/10.1002/2015TC004042.

Wildman, M., Brown, R., Persano, C., Beucher, R., Stuart, F.M., Mackintosh, V., Gallagher, K., Schwanethal, J., Carter, A., 2017. Contrasting Mesozoic evolution across the boundary between on and off craton regions of the south African plateau inferred from apatite fission track and (U-Th-Sm)/he thermochronology. J. Geophys. Res. Solid Earth 122, 1517–1547. https://doi.org/10.1002/2016JB013478.

Wildman, M., Gallagher, K., Chew, D., Carter, A., 2021. From sink to source: using offshore thermochronometric data to extract onshore erosion signals in Namibia. Basin Res. 33, 1580–1602. https://doi.org/10.1111/bre.12527.

Zachos, J.C., Dickens, G.R., Zeebe, R.E., 2008. An early Cenozoic perspective on greenhouse warming and carbon-cycle dynamics. Nature 451, 279–283. https://doi.org/10.1038/nature06588.